Aberrant cortical activity, functional connectivity, and neural assembly architecture after photothrombotic stroke in mice

Mischa V. Bandet,[1,2,3] and Ian R. Winship[1,2,3*]

[1]Neuroscience and Mental Health Institute
[2]Neurochemical Research Unit
[3]Department of Psychiatry
University of Alberta, Edmonton, Alberta T6G 2B7, Canada

Keywords: stroke**;** photothrombosis; two-photon; calcium imaging; gcamp; somatosensory cortex; neural assemblies; ensembles; limb-associated

Running Title: Aberrant cortical activity, functional connectivity and neural assembly architecture after stroke

***Corresponding Author:**
Dr. Ian R. Winship
Professor
Department of Psychiatry
12-127 Clinical Sciences Building
University of Alberta
Edmonton, AB
Canada, T6G 2G3
Phone: 780-492-8658
Fax: 780-492-6841
iwinship@ualberta.ca

Abstract

Despite substantial recent progress in mapping the trajectory of network plasticity resulting from focal ischemic stroke, there is mixed evidence for changes in neuronal excitability and activity within the peri-infarct cortex of mice. Most of these data have been acquired from anesthetized animals, acute tissue slices, or immunoassays on extracted tissue, and thus may not reflect cortical activity dynamics in the intact cortex of an awake animal. Here, *in vivo* two-photon calcium imaging in awake, behaving mice was used to longitudinally track cortical activity, network functional connectivity, and neural assembly architecture for 2 months following photothrombotic stroke targeting the forelimb somatosensory cortex. This model is associated with sensorimotor recovery over the weeks following stroke, allowing us to relate network changes to behavior. Our data revealed spatially restricted but long-lasting alterations in somatosensory neural networks. Specifically, we demonstrate significant and long-lasting disruptions in neural assembly architecture concurrent with a deficit in functional connectivity between individual neurons. Reductions in neuronal spiking in peri-infarct cortex were transient but predictive of impairment in skilled locomotion measured in the tapered beam task. Notably, altered neural networks were highly localized, with assembly architecture and neural connectivity relatively unaltered a distance outside the peri-infarct cortex, even in regions demonstrated to be the site of functional remapping of the forelimb somatosensory representation in anaesthetized preparations. Thus, using longitudinal two photon microscopy in awake animals, these data show a complex spatiotemporal relationship between peri-infarct neuronal network function and behavioral recovery that is more nuanced than functional remapping in response to strong sensory stimulation under anesthesia.

Introduction

Investigations of the excitability of neurons in the peri-infarct cortex during recovery from ischemic stroke have yielded a complex and at times contradictory data set. Peri-infarct hyper-excitability was suggested by data from anesthetized rats that exhibited elevated spontaneous multiunit firing within peri-infarct regions 3-7 days after stroke [1]. Similarly, downregulated GABAergic inhibition in peri-infarct cortex [1–6], degeneration of parvalbumin-positive inhibitory interneurons [3,7], decreased paired pulse inhibition [8–10], increased NMDA receptor mediated excitation [11,12], and a downregulation of KCC2 [13–17] have suggested that the peri-infarct cortex is hyper-excitable during recovery, contributing to increased risk of epileptogenesis in the post stroke brain [13,18]. Conversely, several groups have reported that the sensory-evoked responsiveness of the peri-infarct cortex is diminished during recovery from focal photothombotic stroke [19–25]. Even after months of recovery following forelimb (FL) representation targeted stroke, the remapped representation of the FL has been shown to display prolonged modes of activation with lower amplitude [19] and reduced temporal fidelity [23].

Almost all studies that have examined post-stroke cortical responsiveness have used surgical preparations with anesthetized animals. Anesthesia disrupts cortical activity dynamics and functional connectivity between cortical areas [26–30], and has been shown to reduce the magnitude and spread of cortical activation from sensory stimuli [31–39]. It further reduces the potential contribution of corollary discharge and reafference due to voluntary action in modulating sensory input and cortical responses [40]. It has also recently been shown that the propagation pattern of cortical activity differs between evoked and spontaneous activity, with spontaneous activity showing more complex trajectories and lower activity amplitudes [41].

81 Somatosensory responses are known to be modulated by the relevance of stimuli to behavior and
82 task performance [42–47], and by corollary feedback during [48], or even before [49–51], the
83 onset of movement. Together, these studies point to a complex, interconnected system that
84 modulates the activity of somatosensory networks in the awake behaving animal that is either not
85 present, or is altered, in studies of evoked cortical activity under the anesthetized state. While
86 monitoring cortical activity in awake mobile animals presents methodological complexity, it
87 avoids confounds associated with the anesthetized state and provides unique insight into
88 evolving patterns of network activity that may be unique to the awake state.
89
90 To investigate neural activity patterns during stroke recovery while avoiding the potential
91 confounds of anesthesia, the present work used two photon Ca^{2+} imaging within and distal to the
92 peri-infarct region of a focal photothrombotic stroke lesioning the FL primary somatosensory
93 cortex in mice. We used awake, freely behaving but head-fixed mice in a mobile homecage to
94 longitudinally measure cortical activity, then used computational methods to assess functional
95 connectivity and neural assembly architecture at baseline and each week for 2 months following
96 stroke. Behavioral recovery from stroke was measured in the same animals on a tapered beam
97 task and string pull task to determine the time course of sensorimotor deficits related to changes
98 in cortical activity and network architecture. Our goal was to use longitudinal imaging and
99 advanced computational analyses to define network changes in somatosensory cortex associated
100 with sensorimotor recovery. We show that despite disturbances to the widefield topology and
101 amplitude of the sensory-evoked FL map (acquired under anesthetic), it is only within the
102 immediate peri-infarct region after FL targeted stroke that neural activity, functional
103 connectivity, and neural assembly architecture are disrupted. We demonstrate that the peri-

104 infarct somatosensory cortex displays a marked reduction in neural assembly number, an
105 increase in neural assembly membership, and persistent alterations in assembly-assembly
106 correlations, and that this occurs alongside transient deficits in both functional connectivity and
107 neural activity. Notably, we show that reduced neuronal spiking is strongly correlated with a
108 deficit in motor performance on the tapered beam task. Surprisingly, we also show that
109 measurable deficits in neuronal activity, functional connectivity, and neural assembly
110 architecture are absent within distal cortex as little as 750 µm from the stroke border, even in
111 areas identified by regional imaging as locations of sensory-evoked FL representational
112 remapping.
113

114 **Results**

115 The experimental timeline is illustrated in Fig 1A. Adult Thy1-GCaMP6S mice were
116 implanted with chronic cranial windows and habituated on the floating homecage, tapered beam
117 and string pull task (Fig 1A-C). The cFL and cHL somatosensory areas were mapped on the
118 cortex using widefield Ca^{2+} imaging of stimulus-evoked activity (Fig 1D, 2A, see methods).
119 Regions of interest for longitudinal awake two-photon Ca^{2+} imaging of cellular activity (Fig 1E)
120 were chosen based on pre-stroke widefield Ca^{2+} limb mapping (Fig 2) acquired under isoflurane
121 anaesthesia. The first imaging region of interest was located at the boundary of the pre-stroke
122 cFL and cHL somatosensory maps (termed "peri-infarct" region based on its proximal location
123 to the photothrombotic infarct after stroke) and the second region as lateral to the pre-stroke cHL
124 map (termed "distal" region due to its distance from the stroke boundary). These regions were
125 imaged at baseline, and each week following photothrombotic stroke. Notably, these regions of
126 interest incorporated the predicted areas of remapping for the limb associated somatosensory

127 representations after focal cFL cortex stroke based on previous studies [25,52]. Photothrombosis
128 was directed to the cFL somatosensory representation identified by regional imaging. Resulting
129 infarcts lesioned this region, and borders could be defined by a region of hyperfluorescence 1
130 week post-stroke (Fig 1D, Top). Within the peri-infarct imaging region, cellular dysmorphia and
131 swelling was visually apparent in some cells during two photon imaging 1 week after stroke, but
132 recovered over the 2 month post-stroke imaging timeframe (Fig 1D, Bottom). Morphological
133 changes did not occur in the more distal imaging region lateral to the cHL.
134

135 **Altered sensory-evoked widefield Ca^{2+} maps after stroke**

136 Regional remapping occurs over the weeks following focal cortical stroke [25,52]. Here,
137 widefield Ca^{2+} imaging of the cranial window in isoflurane anaesthetized mice was performed
138 during piezoelectric stimulation of the contralateral limbs prior to stroke, and at the 8 week post-
139 stroke timepoint (Fig 2A, see methods), to define regional sites for cellular Ca^{2+} imaging and to
140 monitor mesoscale changes to somatosensory evoked cortical representations. Fig 2A shows
141 representative montages from a stroke animal illustrating the cortical cFL and cHL Ca^{2+}
142 responses to 1s, 100Hz limb stimulation of the contralateral limbs at the pre-stroke and 8 week
143 post-stroke timepoints. The location and magnitude of the cortical responses changes drastically
144 between timepoints, with the cFL remapping posterior to its pre-stroke location into the area
145 lateral to the cHL map at 8 weeks post-stroke. We observed a significant decrease in the cFL
146 evoked Ca^{2+} response amplitude in the stroke group at 8 weeks post-stroke compared with the
147 pre-stroke timepoint (Fig 2B). This is in agreement with past studies [19–25], and suggests that
148 cFL targeted stroke reduces forelimb evoked activity across the somatosensory cortex in
149 anaesthetized animals even at late time points 2 months after stroke. We observed a concurrent

150 increase in cFL evoked response area in the stroke group 8 weeks post-stroke (Fig 2C),
151 suggesting broader regional activation in response to cFL stimulation with significant posterior
152 remapping of the FL representation (Fig 2D). There were no group differences between stroke
153 and sham groups in cHL evoked intensity, area, or map position (data not shown).
154

155 **Impaired performance on tapered beam but not string pull after focal somatosensory**
156 **stroke**

157 Post-stroke sensorimotor impairment was measured on the tapered beam task and string
158 pull task. In the tapered beam, errors (slips off the beam), indicative of post-stroke impairment,
159 were tracked as the number of left (affected) side slips, right (non-affected) side slips, and the
160 distance to first slip (Fig 3A). We observed a significant interaction between stroke and time
161 after stroke in the number of left side (contralesional) slips (Fig 3B), with *post-hoc* tests
162 confirming a significant increase in left side slips at the 1 week timepoint for stroke animals
163 compared the pre-stroke timepoint ($P = 0.0125$) and in stroke animals compared to sham ($P =$
164 0.0435). Consistent with the unilateral nature of the photothrombotic damage to the cortex in this
165 study, no main effect or interaction was seen in the number of right side slips (Fig 3C). A
166 statistical trend ($P = .0979$) towards a main effect of group was observed in the normalized
167 distance to first slip (Fig 3D). These results are consistent with a transient deficit in motor
168 behavior on the tapered beam during the first week after stroke induced by focal cortical lesion to
169 the sensorimotor cortex [53,54], as opposed to more sustained deficits observed in models of
170 middle cerebral artery occlusion [55,56]. In contrast to previous studies investigating string pull
171 after stroke [57], we did not detect a significant effect of photothrombosis on any kinematic
172 parameters during string pulling (Fig S1).

173 **Firing rate of neurons in the peri-infarct cortex correlates with performance on the tapered**
174 **beam task**

175 The firing rate of cortical somatosensory neurons in our awake behaving animals (Fig
176 4A) was calculated using a custom Matlab algorithm to identify 'significant' calcium transients
177 [58,59] and the mean firing rate of the sampled neural population during periods of movement
178 and periods of rest in the mobile homecage. The normalized average firing rate in the peri-infarct
179 region during recovery during movement and rest is illustrated in Figures 4B and 4C,
180 respectively. A significant interaction between stroke group and recovery time on firing rate was
181 detected at rest (Fig 4C), though a qualitative (but not statistically significant) reduction in firing
182 rate at 1 week was also apparent during movement (Fig 4B). Notably, normalized firing rate at 1
183 week post-stroke during movement and at rest were significantly negatively correlated with the
184 number of left slips in the tapered beam at the same 1 week timepoint ($R^2 = 0.5326$, $P = 0.002$
185 and $R^2 = 0.4346$, $P = 0.0075$, respectively) (Fig 4D and 4E). No main effects or significant
186 interactions were observed in the distal imaging region, though a statistical trend (P=0.0667)
187 towards a main effect of group was observed during animal movement (Fig 4F). Normalized
188 firing rate during movement at 1 week within the distal region was not significantly correlated
189 with left slips on the tapered beam at the same timepoint ($R^2 = 0.0637$, $P = 0.3286$) (Fig 4H). A
190 statistical trend suggesting a negative correlation between normalized firing rate at rest and left
191 slips was observed in the distal cortex ($R^2 = 0.2320$, $P = 0.0503$) (Fig 4I). These results run
192 contrary to previous reports of increased multi-unit activity as early as 3-7 days after focal
193 photothrombotic stroke in the peri-infarct cortex [1], and indicate decreased neuronal spiking 1
194 week after stroke in regions immediately adjacent the infarct that is strongly related to
195 sensorimotor impairment. While the majority of neuronal activity occurred during movement,

196 correlations between firing rate and animal movement were low and did not vary between stroke
197 and sham groups (Fig S2).
198
199 **Altered functional connectivity in the peri-infarct somatosensory cortex**
200 Studies in humans and animals using mesoscale imaging methods indicate that stroke
201 disrupts functional connectivity between widespread cortical regions [26,60–70]. However, few
202 studies have examined functional connectivity at the level of local neural populations after focal
203 stroke [71,72], and none have examined the primary somatosensory cortex. To define functional
204 connectivity in local neural networks within the peri-infarct somatosensory cortex, we plotted the
205 functional connectivity of the neural population in terms of the strength of their cell-cell
206 correlations (Fig 5) and quantified the properties of these connections (Fig 6). We observed a
207 significant loss of functional connectivity as early as 1 week after stroke within the peri-infarct
208 region. This was visually apparent in the stroke group functional connectivity plots at the 1 week
209 timepoint (Fig 5A and 5B) compared to the same location in sham animals (Fig 5E and 5F).
210 Notably, no profound loss of average functional connectivity is visually apparent in the distal
211 region map in the stroke (Fig 5C and 5D) or sham (Fig 5G and 5H) groups. Within the peri-
212 infarct region, we observed a statistical trend (P=.0551) towards a main effect of stroke in the
213 normalized average number of all significant functional connections per neuron (Fig 6A) and a
214 main effect of stroke group on strong connections (r>.03) per neuron (Fig 6B). Significant
215 connections were reduced by stroke, and *post-hoc* tests confirmed fewer significant connections
216 1 week after stroke relative to sham controls. No main effects or interactions between stroke and
217 time were identified in connectivity or significant connections in distal regions of interest (Fig
218 6D and 6E, respectively), highlighting the regional specificity of these network changes relative

219 to the infarct and the original forelimb functional representation. The alterations in significant
220 connections between neurons in peri-infarct parallel a persistent deficit in functional connectivity
221 lasting up to 30 days that was identified within the primary and supplementary motor cortex of
222 mice using in vivo imaging after focal motor cortex stroke [71,72]. Surprisingly, network
223 density, defined as the ratio of measured significant functional network connections to the
224 number of total possible network connections if all neurons were interconnected, was not
225 decreased in either peri-infarct or distal regions in our study (Fig 6C and 6F, respectively). This
226 is in contrast with previous research in the primary and supplementary motor cortex after focal
227 motor cortex stroke that has demonstrated deficits in network density lasting up to 3 weeks post-
228 stroke [72].
229
230 **Neural assembly structure is disrupted in the peri-infarct region after stroke**
231 The neural assembly hypothesis defines coordinated activity in groups of neurons as the
232 basis for the representation of external and internal stimuli within the brain [73–75]. Likewise,
233 perturbations within the structure and function of assemblies may signify aberrant processing of
234 stimuli within neural networks, and is believed to play a significant role in the dysfunction
235 observed in brain damage and neuropsychiatric diseases [74]. Although the use of sophisticated
236 methods for detecting neural assemblies in large populations of neurons has gained increasing
237 popularity with the advent of large population recordings using Ca^{2+} imaging [76], no previous
238 studies have determined the longitudinal effects of stroke on the architecture of neural
239 assemblies in cortex. To determine if focal stroke to the cFL cortex affects the properties of
240 neural assemblies, we used a PCA-Promax procedure [58,59,76] for neural assembly detection to
241 determine assembly size, population membership, assembly quantity, and overlap in assembly

242 membership. The PCA-Promax method for determining neural assemblies allows neurons to
243 participate in more than a single assembly [58,59], a property necessary to examine the ability of
244 neural assemblies to dynamically form with varying members of the population for only brief
245 periods of time [58,59,76]. Fig 7 shows representative cellular Ca^{2+} fluorescence images with
246 neural assemblies color coded and overlaid for each timepoint for the peri-infarct imaging region
247 and for the distal imaging region for an example stroke and sham animal (Fig 7A and 7B,
248 respectively). We observed a significant main effect of stroke group on the number of assemblies
249 (Fig. 8A) after stroke in the peri-infarct imaging region, representing an overall reduction in
250 assemblies. *Post-hoc* comparisons confirmed significantly reduced number of assemblies 1 and 4
251 weeks after stroke relative to sham controls (Fig 8A). A significant main effect on the
252 normalized number of neurons per assembly was detected, reflecting increased membership in
253 each assembly that peaked 1 week after stroke (Fig 8B). We observed a statistical trend ($P =$
254 0.0729) suggesting a higher average percent of the population per assembly (Fig 8C). These data
255 suggest that after stroke, neurons in peri-infarct cortex are functionally grouped into few distinct
256 assemblies, with more neurons per assembly and more of the local network in the same
257 assembly. For the distal imaging region, no differences in neural assembly properties were
258 observed between the stroke and sham groups (Fig 8D-E).
259
260 **Correlation between neural assembly activations is increased after stroke**
261 If differential activation of neural assemblies in the naïve brain relates to representation
262 of different aspects of the external world [58,73,75,77], then changes in the relationship between
263 the activation patterns of assemblies may predict disrupted processing of sensory information
264 within neural networks and how these networks differentially represent external stimuli. An

265 increase in assembly size and reduction in assembly number might reflect a mechanism to
266 replace lost function and increase somatic sensitivity, but may come at the cost of reduced
267 stimulus specificity/fidelity within the network. The activation magnitude of assemblies can be
268 correlated between assemblies over the recording period (Fig 9A). A significant main effect of
269 stroke was detected, reflecting an increase in the average correlation coefficient for significantly
270 correlated assembly-assembly pairs after stroke in the peri-infarct, but not distal cortex, when
271 compared to sham (Fig 9B, 9C). This increased tendency for functionally connected assemblies
272 to be co-active after stroke may reduce the signal to noise ratio for stimulus representation within
273 the network and may reduce stimulus specificity within peri-infarct cortex. While assembly
274 activations were often correlated with movement or rest periods (Fig S3), and 60% of assemblies
275 in both the peri-infarct and distal regions were significantly correlated with animal movement at
276 all time points (S3C and S3E, respectively), stroke did not change the average correlation
277 between assembly activation and animal movement in either the peri-infarct (S3B Fig) or distal
278 region (S3D Fig).
279

280 **Discussion**

281 Here, we used longitudinal two photon calcium imaging of awake, head-fixed mice in the
282 mobile homecage to examine how focal photothrombotic stroke to the forelimb sensorimotor
283 cortex alters the activity and connectivity of neurons adjacent and distal to the infarct. Consistent
284 with previous studies using intrinsic optical signal imaging, mesoscale imaging of regional
285 calcium responses (reflecting bulk neuronal spiking in that region) showed that targeted stroke to
286 the somatosensory cFL representation completely disrupts the sensory evoked forelimb
287 representation in the infarcted region. Functional remapping of this representation occurred over

288 8 weeks after injury, with new sensory evoked spiking found primarily in a region lateral to the
289 cHL representation. Mesoscale calcium imaging allows direct measurement of aggregate
290 neuronal spiking, and remapped cortex exhibited reduced amplitudes of sensory-evoked activity
291 with a broader, less defined cortical map relative to sham. Longitudinal two-photon calcium
292 imaging in awake animals was used to probe single neuron and local network changes adjacent
293 the infarct and in this distal remapped region. This imaging revealed a decrease in firing rate at 1
294 week post-stroke of neurons only in the peri-infarct regions that was significantly negatively
295 correlated with the number of errors made with the stroke-affected limbs on the tapered beam
296 task. Peri-infarct cortical networks also exhibited a reduction in the number of functional
297 connections per neuron and a sustained disruption in neural assembly structure, including a
298 reduction in the number of assemblies and an increased recruitment of neurons into functional
299 assemblies. Elevated correlation between assemblies within the peri-infarct region peaked 1
300 week after stroke and was sustained throughout recovery. Notably, distal networks in the region
301 associated with functional remapping in anaesthetized preparations was largely undisturbed.
302
303 ***Cortical plasticity after stroke***
304 Plasticity within and between cortical regions contributes to partial recovery of function
305 and is proportional to both the extent of damage, as well as the form and quantity of
306 rehabilitative therapy post-stroke [78,79]. A critical period of highest plasticity begins shortly
307 after the onset of stroke, is greatest during the first few weeks, and progressively diminishes over
308 the weeks to months after stroke [19,80–84]. Functional recovery after stroke is thought to
309 depend largely on the adaptive plasticity of surviving neurons that reinforce existing connections
310 and/or replace the function of lost networks [25,52,85–87]. This neuronal plasticity leads to

311 somatosensory and motor functional remapping to adjacent areas of the cortex and altered
312 topographical organization, as observed here. The driver for this process has largely been
313 ascribed to a complex cascade of intra- and extra-cellular signaling that ultimately leads to
314 plastic re-organization of the microarchitecture and function of surviving peri-infarct tissue
315 [52,78,82,86,88–90]. Consistent with our findings, structural and functional remodeling is
316 dependent on the distance from the stroke core, with closer tissue undergoing greater re-
317 organization than more distant tissue (for review, see [52]).
318
319 Previous research examining the region at the border between the cFL and cHL
320 somatosensory maps has shown this region to be a primary site for functional remapping after
321 cFL directed photothrombotic stroke, resulting in a region of cFL and cHL map functional
322 overlap [25]. Within this overlapping area, neurons have been shown to lose limb selectivity 1
323 month post-stroke [25]. This is followed by the acquisition of more selective responses 2 months
324 post-stroke and is associated with reduced regional overlap between cFL and cHL functional
325 maps [25]. Notably, this functional plasticity at the cellular level was assessed using strong
326 vibrotactile stimulation of the limbs in anaesthetized animals. Our findings using longitudinal
327 imaging in awake animals show an initial reduction in firing rate at 1 week post-stroke within
328 this region that was predictive of functional impairment in the tapered beam task. This transient
329 reduction may be associated with reduced or dysfunctional thalamic connectivity [91–93] and
330 reduced transmission of signals from hypo-excitable thalamo-cortical projections [94].
331 Importantly, the strong negative correlation we observed between the normalized firing rate of
332 the neural population within the peri-infarct cortex and the number of errors on the affected side,
333 as well as the quick recovery of firing rate and tapered beam performance, suggests this peri-

334 infarct cortex activity within the peri-infarct region contributes to the impairment and recovery.
335 This common timescale of neuronal and functional recovery also coincides with angiogenesis
336 and re-establishment of vascular support for peri-infarct tissue [81,95–98].
337
338 ***Altered network connectivity after stroke***
339 A highly distributed network of neural circuits forms the basis of information flow in the
340 mammalian brain [99,100]. Many disease states are thought to result in disturbances in neural
341 dynamics and connectivity of these networks due to a process of randomization that affects the
342 network nodes and connections, leading to degraded functional performance of the networks
343 [100,101]. Most studies looking at the functional connectivity of cortical networks after stroke
344 have focused on connectivity between cortical regions and few have looked at functional
345 connectivity within neural populations at the single neuron level within a region of cortex. Our
346 finding of a decreased number of functional connections per neuron in the peri-infarct
347 somatosensory cortex are consistent with recent research that demonstrated a decrease in the
348 total number of functional connections for both inhibitory cells [71] and excitatory cells [71,72]
349 in the motor and premotor cortex approximately 1 week after focal sensorimotor stroke.
350 Reductions in strong functional connections between neurons in our experiments peaked 1 week
351 after stroke, with only partial recovery over the next 7 weeks. These changes were restricted to
352 peri-infarct cortex, and were not observed in regions associated with functional remapping in
353 response to vibrotactile stimulation under anesthesia. As the cumulative total number of
354 functional connections within a neural network is dependent on the number of cells measured
355 from the population, it is possible that a decrease in the number of connections at early
356 timepoints in both studies may either reflect a loss of neurons and/or the functional silencing of

357 neurons within the imaged areas. Unlike Bechay et al. [72], connection density (as % of max
358 possible connections) did not decrease in either the peri-infarct somatosensory cortex or distal
359 somatosensory cortex after stroke in our study. Thus, we observed a significant reduction in the
360 number of strong functional connections between neurons, but not a reduction in the density of
361 connections. It is notable that the peak deficit in peri-infarct functional connectivity in our study
362 occurs simultaneously with reduced neuronal firing and sensorimotor impairment. Early
363 disruption has been reported in anaesthetized animals, and our data in awake animals
364 demonstrates that early network changes may be a key contributor to dysfunction, and a
365 restoration of spiking in peri-infarct regions is related to recovery [19–25].
366
367 ***Altered network dynamics after stroke***
368 According to the cell assembly hypothesis, transient synchronous activation of distributed
369 groups of neurons organize into "neural assemblies" that underly the representation of both
370 external and internal stimuli in the brain [73]. These assemblies have been demonstrated in the
371 mammalian [102–111] and zebrafish [58,112–114] brain, and are often similar in presentation
372 between spontaneous and sensory evoked activations [58,102,107,115,116]. Indeed, the
373 similarity between spontaneous assemblies and sensory evoked assemblies tends to increase
374 during development [102], potentially illustrating the "sculpting" of neural circuits towards
375 commonly encountered sensory stimuli. To date, however, no study has examined changes to the
376 architecture of neural assemblies on the level of single cells within neural networks of the
377 somatosensory cortex in the post-stroke brain. Our data shows a transient decrease in the number
378 of assemblies and an increase in the number of neurons per assembly for the peri-infarct cortex.
379 If assemblies within peri-infarct somatosensory cortex contribute to differential processing of

380 distinct elements of sensory experience, a loss in the number of assemblies may contribute to a
381 loss in sensory range, as is observed in human stroke patients [117–121]. Although there have
382 been calculations on the typical size of cell assemblies in several regions of the brain as a
383 percentage of the network population (for review, see [73]), whether there is an optimal number
384 of assemblies or optimal membership size of a neural assembly for a particular neural population
385 is currently unknown. It is possible that a decrease in the number of assemblies and an increase
386 in the membership of neurons in remaining assemblies may signify inefficient or ineffective
387 forms of sensory processing. Likewise, it has been shown that electrical stimulation of single
388 somatosensory neurons is sufficient to bias animal behavior towards a desired behavioral
389 response [122,123], thereby suggesting that a sparse neural code may be sufficient for sensation.
390 It has also been argued that minimizing correlation within the neural population serves to reduce
391 representational redundancy and improves representational efficiency [124,125], thereby
392 suggesting that fewer assemblies, with each containing more members, may be an inefficient
393 form of representational coding for sensory information. Furthermore, we observed a persistent
394 increase in the correlation between the activations of assemblies in the peri-infarct cortex that
395 peaks 1 week post-stroke. Co-activation of multiple assemblies simultaneously may decrease the
396 signal-to-noise ratio of the representational information that each specific assembly holds. It may
397 further reduce efficient information transfer within and between cortical networks, and may
398 relate to prolonged modes of somatosensory activation [19] and reduced fidelity in response to
399 sensory stimuli observed in mouse models of focal FL stroke [23].
400
401 Consistent with previous research [25], we show that at the 8 week timepoint after cFL
402 photothrombotic stroke the cFL representation, identified by mechanical limb stimulation under

403 anaesthesia, is shifted posterior from its pre-stroke location into the area lateral to the cHL map.
404 Notably, our distal imaging region was directly within this remapped cFL area. Despite this, we
405 found little change in the normalized firing rate in either moving or resting states in this region.
406 This is in contrast to past research in anesthetized animals that indicated an increase in sensory-
407 evoked activity within this area lateral to the cHL representation 1-2 months after focal cFL
408 stroke [25]. Moreover, there was no indication that the cFL remapping into this distal area lateral
409 to the cHL map resulted in any detectable change to the level of population correlation,
410 functional connectivity, assembly architecture or assembly activations as compared to sham.
411 Notably, sensory-evoked activity for regional mapping was evoked via strong vibrotactile (1s,
412 100Hz) limb stimulation. The combination of anesthetic and strong stimulation may unmask
413 connectivity in distal regions during anesthesia that is not apparent during more naturalistic
414 stimulation during awake locomotion or rest. Nonetheless, these results support a limited spatial
415 distance over which the peri-infarct area exhibits network functional deficits. These results are
416 also consistent with a spatial gradient of plasticity factors that are generally enhanced with closer
417 proximity to the infarct core [82,86,88,89].
418
419 In summary, this work demonstrates that the peri-infarct region near to the stroke core
420 displays decreased neuronal activity 1 week after stroke that is predictive of poor performance on
421 the tapered beam task. Moreover, local neuronal networks adjacent the stroke exhibited
422 reductions in functional connectivity and sustained alterations in the structure of neuronal
423 assemblies, suggesting that focal injury leads to long lasting alterations in functional connectivity
424 between neurons in local neuronal networks. Interestingly, altered connectivity and neuronal
425 assembly structure was not detected in more distal cortical regions, even though those regions

426 were associated with functional remapping of somatosensory-evoked activity in response to
427 vibrotactile limb stimulation under anaesthesia. The persistence of these distal networks during
428 recovery highlights the importance of awake imaging and naturalistic stimuli to fully define
429 functional network changes during recovery from nervous system injury. The restriction of these
430 network changes to peri-infarct cortex could reflect the small penumbra associated with
431 photothrombotic stroke, and future studies could make use of stroke models with larger
432 penumbral regions, such as the middle cerebral artery occlusion model. Larger injuries induce
433 more sustained sensorimotor impairment, and the relationship between neuronal firing,
434 connectivity, and neuronal assemblies could be further probed relative to recovery or sustained
435 impairment in these models.
436

437 ## Materials and Methods

438 **Animals**

439 Three to nine month old Thy1-GCaMP6S mice (Strain GP4.3, Jax Labs) (N=16 stroke
440 (average age: 5.4 months), 5 sham (average age: 6 months)) were used in this study. Mice were
441 group housed in standard laboratory cages in a temperature-controlled room (23ºC), maintained
442 on a 12 hr light/dark cycle, and given standard laboratory diet and water *ad libitum*. Cages were
443 randomly assigned to stroke or sham groups such that stroke and sham mice did not co-habitate
444 the same cages. Animal weight was monitored daily during the entirety of the experiment. All
445 experiments were approved by the University of Alberta's Health Sciences Animal Care and Use
446 Committee and adhered to the guidelines set by the Canadian Council for Animal Care. Animals
447 were euthanized through decapitation under deep urethane anesthesia following the end of the
448 final imaging session.

449

450 **Chronic cranial window implantation**

451 Mice were implanted with a chronic cranial window [126] four weeks prior to the first
452 imaging time point (Fig 1B). A surgical plane of anesthesia was achieved with 1.5% isofluorane.
453 Body temperature was measured using a rectal probe and maintained at 37±0.5ºC. Mice were
454 administered 0.15 mL of saline subcutaneously to maintain hydration levels. Dexamethasone (2
455 ug/g) was given subcutaneously to prevent cortical swelling and hemorrhaging during the
456 craniotomy procedure. The skull was exposed by midline scalp incision and the skin retracted.
457 The skull was gently scraped with a scalpel to remove the periosteum. Grooves were scraped into
458 the skull surface to improve adhesion of dental cement to the skull. A 4 x 4 mm region of the
459 skull overlying the right hemisphere somatosensory region was thinned to 25-50% of original
460 thickness using a high-speed dental drill (~1-5mm lateral, +2 to -2 mm posterior to bregma). A
461 dental drill was used to progressively thin the overlying skull until the bone could be removed
462 with forceps, leaving the dura intact. The exposed cortical surface was bathed in sterile saline
463 solution. A 5mm diameter coverslip was held in place over the craniotomy and its edges attached
464 to the skull using cyanoacrylate glue. A metal headplate was positioned and secured to the skull
465 using dental cement. Animals were injected subcutaneously with buprenorphine (1.0 mg/kg),
466 removed from the isofluorane, and allowed to recovery in a temperature-controlled recovery
467 cage. Mice were returned to their home cage once recovered and monitored daily for weight and
468 post-surgical signs for the duration of the chronic experiment. Mice were allowed to recover for
469 a period of two weeks after window implantation prior to beginning behavior and task
470 habituation (Fig 1C). Animals were excluded at the 2 week post-implantation timepoint if their
471 cranial window became cloudy or non-imageable.

472

473 **Tapered beam task habituation, testing and analysis**

474 Methods for tapered beam habituation and automated recording and analysis have been
475 described previously [53], with minor modification as follows. Nesting material from the
476 homecage was placed inside of a dark box at the narrow end of the beam to motivate animals to
477 cross the beam. For the first three sessions, mice were placed at the wide end of the beam and
478 allowed to freely explore the beam for a period of 2 minutes, after which the experimenter placed
479 a sheet of paper behind the animal as it crossed the beam to block its return path to the wide end
480 and motivate it to cross to the narrow end with dark box. Once the mouse had reached the dark
481 box with bedding material at the narrow end, they were given 60 seconds within the dark box to
482 associate crossing the beam with reaching the safety of the dark box. The dark box was
483 transported to their respective cage for the animal to further associate reaching the dark box with
484 a safe transition to their cage. On subsequent days, mice were continuously run through the
485 tapered beam for a period of 2 mins each, with a return to their cage after each crossing. On each
486 of the 3 days prior to the first Ca^{2+} imaging session, mice were tested with three crossings of the
487 beam per day to determine baseline crossing performance. Left and right side slips were captured
488 automatically by Raspberry Pi computer attached to touch sensors on the tapered beam, and
489 Python scripts run to determine number of slips for each side and distance to first slip.
490 Performance on the 9 baseline trials were average to determine a singular average baseline
491 performance level. Mice were tested with three trials on each day prior to each weekly post-
492 imaging timepoint to measure changes in performance.

493

494 **String pull task habituation, testing and analysis**

495 Methods for string pull habituation and testing have previously been described [127,128],
496 with modification as follows. For habituation, mice were individually placed in a transparent
497 rectangular cage without bedding and allowed to freely explore for a period of 5 minutes. 20
498 strings with variable length were hung over the edge of the cage. Half of the strings were baited
499 with chocolate flavored sucrose pellets. Mice were removed from the apparatus once all of the
500 strings had been pulled into the cage, or once 20 minutes had elapsed. On subsequent days 2 and
501 3, mice were again placed in the cage with 20 strings to pull. Following this 3-day habituation,
502 from days 4-14 mice were habituated in an alternate transparent string pull box with high sides
503 and transparent front face for video recording. Within this second habituation box, mice received
504 3 trials with baited strings hung facing the recording camera. The session was terminated when
505 the animal had pulled all three strings or once 20 minutes had elapsed, and the apparatus
506 prepared for the next mouse. On the last day prior to the first Ca^{2+} imaging session, 3 trials of
507 string pull from each mouse were recorded with the use of a GoPro Hero 7 Black (60 fps,
508 1920×1080 pixels). Mice were re-tested with this same 3 string protocol the day prior to each of
509 their weekly imaging timepoints. Video recordings were analyzed using a semi-automated
510 Matlab string pull package [128]. Reach and withdraw movement scaling for the left and right
511 paw was calculated by running a Pearson's correlation between the series of Euclidian distances
512 that the paw travelled during each of the reach or withdraw movements during the string pull and
513 correlating with the peak speed of the paw during each of the respective reaches or withdraws
514 [129]. A value of 1 indicates a strong linear relationship between longer reach/withdraw paw
515 movement distance and greater peak speed that the paw obtained. Paw reach distance was
516 calculated as the average distance that the paw travelled during each reach movement. Path

517 circuity is used as a measure of how direct of a path a reach or withdraw movement takes
518 between its starting and end points and is calculated as the total distance travelled divided by the
519 Euclidian distance between the start and end points [129]. The greater the path circuity value is
520 above 1, the more the path of the paw deviated from the ideal direct path between the start and
521 end points of the reach/withdraw. A bimanual correlation coefficient was calculated by first
522 detrending the timeseries of Y-axis paw position to remove general changes in the posture of the
523 animal over the course of the string pull attempt, then running a Pearson's correlation between
524 the Y-axis paw position measurements for the right and left paw.
525
526 **Mobile floating homecage habituation and measurement of movement parameters**
527 Methods for floating homecage (Neurotar, Finland) habituation have previously been
528 described [130], with modification as follows. Two weeks after cranial window implantation,
529 each mouse was handled for 5 minutes 3 times per day for the first 2 days to habituate them to
530 handling. For days 3-4, each mouse was handled and repeatedly wrapped and released with a soft
531 cloth for a period of 5 mins 3 times per day in order to habituate to the wrapping procedure. Mice
532 were also given 1 period of 5 minutes each per day to freely explore the floating homecage
533 without being head-restrained. For days 5-8, twice per day the animals were head-restrained in
534 the floating homecage and allowed to move around the floating homecage for a period of 15
535 minutes with the room lights off before being returned to their cage. For days 8-14, twice per day
536 the mice were head-restrained in the floating homecage for 25 minutes with the floating
537 homecage attached to the microscope in the same conditions in which the animals would be
538 imaged on day 15 onwards. On day 14 (one day prior to their first imaging session) baseline
539 performance on the string pull and tapered beam tasks was measured prior to their last

540 habituation in the floating homecage. Animal movement within the homecage during each Ca^{2+}
541 imaging sessions was tracked to determine animal speed and position. Animal speed was
542 thresholded at 30mm/s to determine periods of time in which the animal was moving and periods
543 of rest were determined as speed below 30mm/s.
544
545 **Identification of forelimb and hindlimb somatosensory cortex representations using**
546 **widefield Ca^{2+} imaging of sensory-evoked responses**
547 On day 10 of habituation, mice were anesthetized with 1.25% isofluorane after they had
548 completed all daily task training and floating homecage habituation. Mice were head-fixed on a
549 stereotaxic frame with continuous isofluorane anesthesia. Body temperature was measured using
550 a rectal probe and maintained at 37±0.5ºC. The cortical surface was illuminated with a xenon
551 lamp (excitation band-pass filtered at 450-490nm). Fluorescent emissions were long-pass filtered
552 at 515nm and captured in 12-bit format by a Dalsa Pantera 1M60 camera mounted on a Leica
553 SP5 confocal microscope using a 2.5X objective. The depth of focus was set at 200 μm below
554 the cortical surface. Custom-made piezoceramic mechanical bending actuators were used to elicit
555 oscillatory limb stimulation during widefield Ca^{2+} imaging. The piezo bending actuators
556 comprised a piezo element (Piezo Systems # Q220-A4-203YB) attached to an electrically
557 insulated metal shaft holding a metal U-bend at its end. The palm of the mouse paw was placed
558 within the U-bend, and the U-bend bent to shape to lightly secure the palm. The metal U-bend
559 made contact across a vertical rectangular area of approximately 3x1mm on the palmar and
560 dorsal surface of the hand. Stimulators were driven with square-wave signals from an A-M
561 Systems Model 2100 Isolated Pulse Stimulator. Stimulation alternated between contralateral
562 forelimb (cFL) and contralateral hindlimb (cHL) for up to 40 trials of stimulation of each limb.

563 Placement of actuators was on the glabrous skin of the forepaw or hindpaw, with consistent
564 alignment relative to the flexion of wrist and ankle. Images were captured for 5.0s at 10 Hz (1s
565 before and 4s after stimulus onset; interstimulus interval = 20s). The trials for each limb were
566 averaged in ImageJ software (NIH). 10 imaging frames (1s) after stimulus onset were averaged
567 and divided by the 10 baseline frames 1s before stimulus onset to generate a response map for
568 each limb. Response maps were thresholded at 95% maximal response to determine limb
569 associated response boundaries, merged, and overlaid on an image of surface vasculature to
570 delineate the cFL and cHL somatosensory areas.
571
572 **Calcium imaging**
573 On the day following testing for behavioral performance on the string pull and tapered
574 beam tasks, animals were head-fixed within the mobile homecage and Ca^{2+} imaging was
575 performed. Awake in-vivo two-photon imaging was performed using a Leica SP5 MP confocal
576 microscope equipped with a Ti:Sapphire Coherent Chameleon Vision II laser tuned to 940 nm
577 for GCaMP6S excitation. A Leica HCX PL APO L 20x 1.0NA water immersion objective was
578 used. Images were acquired using Leica LAS AF using no averaging, a zoom of 1.7x and a
579 frame-rate of 25Hz. Images were acquired at 512x512 pixels over an area of 434x434μm,
580 yielding a resolution of 0.848μm per pixel. Two imaging regions were chosen for each animal,
581 with one corresponding to the half-way point between the pre-stroke cFL and cHL
582 somatosensory maps previously determined with widefield Ca^{2+} imaging (the "peri-infarct"
583 imaging region), and the other an imaging region located just lateral to the cHL sensory map (the
584 "distal" imaging region). These regions can be seen in Fig 1D and Fig 2A. Each imaging region
585 was recorded for 15 minutes while simultaneously tracking the animal's movement and position

586 within the mobile homecage. Imaging depth was set between 100-180um below the cortical
587 surface. There were no differences between the stroke group and sham group for movement
588 within the mobile homecage, though both groups displayed an equivalent decrease in the amount
589 of time they spent moving within the 15 minute recording sessions over the course of the 8 week
590 experimental timeline, potentially reflecting continuing habituation over this period.
591
592 **Photothrombotic stroke and sham procedure**
593 After baseline cellular Ca^{2+} imaging, mice were anesthetized using 1.25% isofluorane
594 and head-fixed on a stereotaxic frame with continuous isofluorane anesthesia. Body temperature
595 was measured using a rectal probe and maintained at 37±0.5ºC. The mapped cFL area was used
596 as a guide for a targeted photothrombosis procedure. Briefly, a 2mm diameter hole was punched
597 in black electrical tape and attached onto the glass window to block stray light from illuminating
598 cortical areas outside of the desired region. Rose Bengal (a photosensitive dye) was dissolved in
599 0.01M sterile phosphate buffered saline (Sigma) and injected intraperitoneal (30mg/kg). The cFL
600 cortical area visible through the punched electrical tape was illuminated using a collimated beam
601 of green laser light (532 nm, 17mW) for 20 minutes to photoactivate the Rose Bengal and cause
602 a focal ischemic lesion. Sham controls were treated in the same manner as stroke, however
603 illumination of the laser was omitted.
604
605 **Two-photon image processing and analysis of neuronal activity**
606 Timeseries images (15 minutes per imaging region, 22500 frames per recording, 25fps)
607 were group averaged in groups of 2, then motion corrected using the TurboReg plugin in FiJi
608 with translation only registration [131]. Z-projections within FiJi of the average and standard

609 deviation were used to define neuronal ROI through manual tracing. Using custom written
610 scripts in Matlab 2020b, ROIs were imported and converted into a format suitable for the Ca^{2+}
611 imaging toolbox used for subsequent steps [59]. Neuropil for each ROI was determined by
612 expanding an annular donut around each ROI to calculate the neuropil deltaF/Fo surrounding
613 each ROI. During computation of neuron ROI deltaF/Fo, fluorescence was corrected for neuropil
614 contamination using the formula ($F_{corrected} = F_{raw} - \alpha * F_{neuropil}$) where α was set to 0.4 based on
615 previous studies suggesting that α values between 0.3-0.5 were optimal [132], and with $F_{neuropil}$
616 determined by the peri-somatic donut neuropil fluorescence closely associated with each neuron.
617 A smoothed estimate of the baseline fluorescence was calculated by taking a 30s running average
618 of the 8th percentile of the raw fluorescence, which was then subtracted from the raw
619 fluorescence to remove baseline drift.
620
621 **Ca^{2+} trace deconvolution to determine neuronal transients**
622 To determine significant fluorescent Ca^{2+} transients from the deltaF/Fo of each neuron, a
623 dynamic threshold implementing a Bayesian odds ratio estimation framework for noise
624 estimation was used to determine transients that met the condition of being greater than 98% of
625 the confidence interval for the calculated fluorescent baseline noise, and were compatible with a
626 tau of ~1.8s for GCaMP6S [58,59]. Determination of firing was performed on the neuronal
627 deltaF/Fo traces, as implemented in [58,59], in order to define the Ca^{2+} transient rate and to
628 generate raster plots. This information was used to determine neuronal activity "firing rate" as
629 shown in Fig 4.
630

631 **Neuron-neuron correlation analysis and functional connectivity**

632 Using custom written scripts in Matlab, Pearson product-moment correlation coefficients
633 were calculated between the z-scored Ca^{2+} traces derived from each of the neuronal ROIs in a
634 given optical section. Distance between neuron pairs was calculated from the Euclidean distance
635 between the central points of the neuron ROIs of the image frame. Functional connectivity plots
636 (Fig 5) were generated by plotting neuron ROI centroids as red dots, and lines between them
637 with line weight and color determined by the strength of the correlation between them.
638 Stationary variable block bootstrapping (5000 iterations) was performed as a statistical test for
639 the significance of each pairwise correlation and only correlations that were greater than the 99th
640 percentile of the bootstrap were deemed statistically significant and plotted. Average number of
641 significant connections per neuron was calculated by dividing the number of functional
642 connections that met the bootstrapping threshold by the total number of neurons in the
643 population. Connection density was calculated as percent of max by taking the total number of
644 significant functional connections and dividing by the total potential number of functional
645 connections if every neuron within the population was functionally connected with all other
646 neurons.

647

648 **Determination of neural assemblies and their activity patterns**

649 To evaluate the co-activity patterns of neurons that form putative neural assemblies, a
650 PCA-Promax procedure was applied as previously described [58,59], with a zMax threshold
651 manually selected by the first clear minimum in the distribution of z-scored maximal ROI
652 loadings. Notably, the PCA-Promax procedure relaxes the PCA orthogonality condition using a
653 PROMAX oblique rotation of the PC axes [133], such that assemblies can contain neurons found

654 within other assemblies. Due to this relaxation of the PCA orthogonality condition, assemblies
655 with high overlap whose dot product exceeded 0.6 were merged [133]. All assemblies were
656 compared to surrogate control datasets, and only those assemblies whose members were
657 significantly correlated and synchronous were kept ($p < 0.05$). To determine the co-activity of
658 neurons within assemblies, a matching index was calculated [58,59,134,135]. The matching
659 index quantifies the proportion of neurons within the assembly that are co-activated
660 simultaneously over the timeseries, with a maximal value of 1 indicating perfect overlap in
661 assembly member activation. The significance of each assembly activation over the timeseries
662 was determined by comparing the activation events to a probability distribution based on the size
663 of the assembly, the size of the total population of N ROIs, and with a threshold p-value of <0.05
664 considered to be a statistically significant activation. For cross-correlation of assembly
665 activations with speed (Fig S3) and assembly-assembly correlations (Fig 9), the matching index
666 was first multiplied by the Boolean timeseries of individual assembly activation significance to
667 generate matching index timeseries of significant assembly activations only (presented in Fig S3
668 and Fig 9 as percent of maximal assembly activation). ROIs of assembly members were color
669 coded according to their assembly membership, and overlaid on an averaged fluorescence image
670 to generate assembly plots (Fig 7).
671
672 **Statistical analysis**
673 Multivariate comparisons were made using a mixed-effects model for repeated measures
674 based on a restricted maximum likelihood generalized linear mixed model as implemented in
675 Graphpad Prism 9.0.0, with Bonferroni-Sidak corrections used for *post-hoc* comparisons.
676 Bonferroni-Sidak *post-hoc* testing was used to compare the means of the stroke vs. the sham

group at each timepoint, as well as to identify within group differences by comparing different timepoints within each group. Normalized data was analyzed using multivariate mixed-effects models based on a restricted maximum likelihood generalized linear mixed model, with the "pre" timepoint removed from calculation of main effects, interaction, and *post-hoc* statistical testing. Grubb's test was used to remove data outliers with alpha set to 0.05. All zero time-lag cross-correlations were computed using Pearson's *r*. A stationary bootstrapping procedure was used as a test of the significance of the calculated Pearson's r of each pairwise timeseries comparison. Within the stationary bootstrapping procedure, 5000 iterations were run and an average block length of 23 frames (1.84s) was used based on previous studies indicating ~1.8s as the decay time for GCaMP6S Ca^{2+} sensor within neurons [136,137]. Pairwise r values greater than the 99th percentile of the stationary bootstrap were deemed significant. Non-significant pairwise r values were excluded from analyses of average correlation values. For all statistical comparisons, a *p* value of ≤0.05 was considered statistically significant. A *p* value of ≤0.10 was considered a statistical trend. Data are expressed as the mean ± SEM.

Author Contributions

MVB and IRW designed all experiments. MVB performed experiments and analyzed data. MVB and IRW wrote the manuscript together.

Competing Interests

The authors declare no competing interests.

Data Availability

All data generated or analyzed during this study will be made publicly available on OSF (https://osf.io/wam9j/).

REFERENCES

1. Schiene K, Bruehl C, Zilles K, Qü M, Hagemann G, Kraemer M, et al. Neuronal hyperexcitability and reduction of GABAA-receptor expression in the surround of cerebral photothrombosis. J Cereb Blood Flow Metab Off J Int Soc Cereb Blood Flow Metab. 1996;16: 906–914. doi:10.1097/00004647-199609000-00014

2. Mittmann T, Qü M, Zilles K, Luhmann HJ. Long-term cellular dysfunction after focal cerebral ischemia: in vitro analyses. Neuroscience. 1998;85: 15–27. doi:10.1016/S0306-4522(97)00638-6

3. Neumann-Haefelin T, Staiger JF, Redecker C, Zilles K, Fritschy JM, Möhler H, et al. Immunohistochemical evidence for dysregulation of the GABAergic system ipsilateral to photochemically induced cortical infarcts in rats. Neuroscience. 1998;87: 871–879. doi:10.1016/s0306-4522(98)00124-9

4. Neumann-Haefelin T, Bosse F, Redecker C, Müller HW, Witte OW. Upregulation of GABAA-receptor alpha1- and alpha2-subunit mRNAs following ischemic cortical lesions in rats. Brain Res. 1999;816: 234–237. doi:10.1016/s0006-8993(98)01162-7

5. Qü M, Buchkremer-Ratzmann I, Schiene K, Schroeter M, Witte OW, Zilles K. Bihemispheric reduction of GABAA receptor binding following focal cortical photothrombotic lesions in the rat brain. Brain Res. 1998;813: 374–380. doi:10.1016/s0006-8993(98)01063-4

6. Redecker C, Wang W, Fritschy J-M, Witte OW. Widespread and Long-Lasting Alterations in GABAA-Receptor Subtypes after Focal Cortical Infarcts in Rats: Mediation by NMDA-Dependent Processes. J Cereb Blood Flow Metab. 2002;22: 1463–1475. doi:10.1097/01.WCB.0000034149.72481.BD

7. Luhmann HJ, Mudrick-Donnon LA, Mittmann T, Heinemann U. Ischaemia-induced long-term hyperexcitability in rat neocortex. Eur J Neurosci. 1995;7: 180–191. doi:10.1111/j.1460-9568.1995.tb01054.x

8. Buchkremer-Ratzmann I, Witte OW. Extended brain disinhibition following small photothrombotic lesions in rat frontal cortex. NeuroReport. 1997;8: 519–522.

732 9. Domann R, Hagemann G, Kraemer M, Freund H-J, Witte OW. Electrophysiological
733 changes in the surrounding brain tissue of photochemically induced cortical infarcts in the
734 rat. Neurosci Lett. 1993;155: 69–72. doi:10.1016/0304-3940(93)90675-B

735 10. Fujioka H, Kaneko H, Suzuki SS, Mabuchi K. Hyperexcitability-associated rapid
736 plasticity after a focal cerebral ischemia. Stroke. 2004;35: e346-348.
737 doi:10.1161/01.STR.0000130990.28734.9c

738 11. Qü M, Mittmann T, Luhmann HJ, Schleicher A, Zilles K. Long-term changes of
739 ionotropic glutamate and GABA receptors after unilateral permanent focal cerebral
740 ischemia in the mouse brain. Neuroscience. 1998;85: 29–43. doi:10.1016/s0306-
741 4522(97)00656-8

742 12. Que M, Schiene K, Witte OW, Zilles K. Widespread up-regulation of N-methyl-D-
743 aspartate receptors after focal photothrombotic lesion in rat brain. Neurosci Lett.
744 1999;273: 77–80. doi:10.1016/s0304-3940(99)00598-4

745 13. Jaenisch N, Liebmann L, Guenther M, Hübner CA, Frahm C, Witte OW. Reduced tonic
746 inhibition after stroke promotes motor performance and epileptic seizures. Sci Rep.
747 2016;6: 26173. doi:10.1038/srep26173

748 14. Jin X, Huguenard JR, Prince DA. Impaired Cl- extrusion in layer V pyramidal neurons of
749 chronically injured epileptogenic neocortex. J Neurophysiol. 2005;93: 2117–2126.
750 doi:10.1152/jn.00728.2004

751 15. Khirug S, Soni S, Saez Garcia M, Tessier M, Zhou L, Kulesskaya N, et al. Protective Role
752 of Low Ethanol Administration Following Ischemic Stroke via Recovery of KCC2 and
753 p75NTR Expression. Mol Neurobiol. 2021;58: 1145–1161. doi:10.1007/s12035-020-
754 02176-x

755 16. Martín-Aragón Baudel MAS, Poole AV, Darlison MG. Chloride co-transporters as
756 possible therapeutic targets for stroke. J Neurochem. 2017;140: 195–209.
757 doi:10.1111/jnc.13901

758 17. Schulte JT, Wierenga CJ, Bruining H. Chloride transporters and GABA polarity in
759 developmental, neurological and psychiatric conditions. Neurosci Biobehav Rev. 2018;90:
760 260–271. doi:10.1016/j.neubiorev.2018.05.001

761 18. Witte OW, Freund HJ. Neuronal dysfunction, epilepsy, and postlesional brain plasticity.
762 Adv Neurol. 1999;81: 25–36.

763 19. Brown CE, Aminoltejari K, Erb H, Winship IR, Murphy TH. In Vivo Voltage-Sensitive
764 Dye Imaging in Adult Mice Reveals That Somatosensory Maps Lost to Stroke Are
765 Replaced over Weeks by New Structural and Functional Circuits with Prolonged Modes of
766 Activation within Both the Peri-Infarct Zone and Distant Sites. J Neurosci. 2009;29:
767 1719–1734. doi:10.1523/JNEUROSCI.4249-08.2009

768 20. Chen S, Mohajerani MH, Xie Y, Murphy TH. Optogenetic analysis of neuronal
769 excitability during global ischemia reveals selective deficits in sensory processing
770 following reperfusion in mouse cortex. J Neurosci Off J Soc Neurosci. 2012;32: 13510–
771 13519. doi:10.1523/JNEUROSCI.1439-12.2012

772 21. Lim DH, LeDue JM, Mohajerani MH, Murphy TH. Optogenetic mapping after stroke
773 reveals network-wide scaling of functional connections and heterogeneous recovery of the
774 peri-infarct. J Neurosci Off J Soc Neurosci. 2014;34: 16455–16466.
775 doi:10.1523/JNEUROSCI.3384-14.2014

776 22. Sigler A, Mohajerani MH, Murphy TH. Imaging rapid redistribution of sensory-evoked
777 depolarization through existing cortical pathways after targeted stroke in mice. Proc Natl
778 Acad Sci. 2009;106: 11759–11764.

779 23. Sweetnam DA, Brown CE. Stroke induces long-lasting deficits in the temporal fidelity of
780 sensory processing in the somatosensory cortex. J Cereb Blood Flow Metab Off J Int Soc
781 Cereb Blood Flow Metab. 2013;33: 91–96. doi:10.1038/jcbfm.2012.135

782 24. Sweetnam D, Holmes A, Tennant KA, Zamani A, Walle M, Jones P, et al. Diabetes
783 Impairs Cortical Plasticity and Functional Recovery Following Ischemic Stroke. J
784 Neurosci. 2012;32: 5132–5143. doi:10.1523/JNEUROSCI.5075-11.2012

785 25. Winship IR, Murphy TH. In vivo calcium imaging reveals functional rewiring of single
786 somatosensory neurons after stroke. J Neurosci Off J Soc Neurosci. 2008;28: 6592–6606.
787 doi:10.1523/JNEUROSCI.0622-08.2008

788 26. Cramer JV, Gesierich B, Roth S, Dichgans M, Düring M, Liesz A. In vivo widefield
789 calcium imaging of the mouse cortex for analysis of network connectivity in health and
790 brain disease. NeuroImage. 2019;199: 570–584. doi:10.1016/j.neuroimage.2019.06.014

791 27. Grandjean J, Schroeter A, Batata I, Rudin M. Optimization of anesthesia protocol for
792 resting-state fMRI in mice based on differential effects of anesthetics on functional
793 connectivity patterns. NeuroImage. 2014;102: 838–847.
794 doi:10.1016/j.neuroimage.2014.08.043

795 28. Jonckers E, Delgado y Palacios R, Shah D, Guglielmetti C, Verhoye M, Van der Linden
796 A. Different anesthesia regimes modulate the functional connectivity outcome in mice.
797 Magn Reson Med. 2014;72: 1103–1112. doi:10.1002/mrm.24990

798 29. Kalthoff D, Po C, Wiedermann D, Hoehn M. Reliability and spatial specificity of rat brain
799 sensorimotor functional connectivity networks are superior under sedation compared with
800 general anesthesia. NMR Biomed. 2013;26: 638–650. doi:10.1002/nbm.2908

801 30. Nasrallah FA, Tay H-C, Chuang K-H. Detection of functional connectivity in the resting
802 mouse brain. NeuroImage. 2014;86: 417–424. doi:10.1016/j.neuroimage.2013.10.025

803 31. Chapin JK, Lin CS. Mapping the body representation in the SI cortex of anesthetized and

804 awake rats. J Comp Neurol. 1984;229: 199–213. doi:10.1002/cne.902290206

805 32. Chen LM, Friedman RM, Roe AW. Optical imaging of SI topography in anesthetized and
806 awake squirrel monkeys. J Neurosci Off J Soc Neurosci. 2005;25: 7648–7659.
807 doi:10.1523/JNEUROSCI.1990-05.2005

808 33. Devonshire IM, Grandy TH, Dommett EJ, Greenfield SA. Effects of urethane anaesthesia
809 on sensory processing in the rat barrel cortex revealed by combined optical imaging and
810 electrophysiology. Eur J Neurosci. 2010;32: 786–797. doi:10.1111/j.1460-
811 9568.2010.07322.x

812 34. Lissek T, Obenhaus HA, Ditzel DAW, Nagai T, Miyawaki A, Sprengel R, et al. General
813 Anesthetic Conditions Induce Network Synchrony and Disrupt Sensory Processing in the
814 Cortex. Front Cell Neurosci. 2016;10: 64. doi:10.3389/fncel.2016.00064

815 35. Ebner FF, Kaas JH. Chapter 24 - Somatosensory System. In: Paxinos G, editor. The Rat
816 Nervous System (Fourth Edition). San Diego: Academic Press; 2015. pp. 675–701.
817 doi:10.1016/B978-0-12-374245-2.00024-3

818 36. Friedberg MH, Lee SM, Ebner FF. Modulation of Receptive Field Properties of Thalamic
819 Somatosensory Neurons by the Depth of Anesthesia. J Neurophysiol. 1999;81: 2243–
820 2252. doi:10.1152/jn.1999.81.5.2243

821 37. Faggin BM, Nguyen KT, Nicolelis MA. Immediate and simultaneous sensory
822 reorganization at cortical and subcortical levels of the somatosensory system. Proc Natl
823 Acad Sci U S A. 1997;94: 9428–9433. doi:10.1073/pnas.94.17.9428

824 38. Moore CI, Nelson SB. Spatio-Temporal Subthreshold Receptive Fields in the Vibrissa
825 Representation of Rat Primary Somatosensory Cortex. J Neurophysiol. 1998;80: 2882–
826 2892. doi:10.1152/jn.1998.80.6.2882

827 39. Nicolelis MA, Chapin JK. Spatiotemporal structure of somatosensory responses of many-
828 neuron ensembles in the rat ventral posterior medial nucleus of the thalamus. J Neurosci.
829 1994;14: 3511–3532. doi:10.1523/JNEUROSCI.14-06-03511.1994

830 40. Crapse TB, Sommer MA. Corollary discharge across the animal kingdom. Nat Rev
831 Neurosci. 2008;9: 587–600. doi:10.1038/nrn2457

832 41. Afrashteh N, Inayat S, Bermudez-Contreras E, Luczak A, McNaughton BL, Mohajerani
833 MH. Spatiotemporal structure of sensory-evoked and spontaneous activity revealed by
834 mesoscale imaging in anesthetized and awake mice. Cell Rep. 2021;37: 110081.
835 doi:10.1016/j.celrep.2021.110081

836 42. Dionne JK, Legon W, Staines WR. Crossmodal influences on early somatosensory
837 processing: interaction of vision, touch, and task-relevance. Exp Brain Res. 2013;226:
838 503–512. doi:10.1007/s00221-013-3462-z

839 43. Johansen-Berg H, Christensen V, Woolrich M, Matthews PM. Attention to touch
840 modulates activity in both primary and secondary somatosensory areas. Neuroreport.
841 2000;11: 1237–1241.

842 44. Nelson AJ, Staines WR, Graham SJ, McIlroy WE. Activation in SI and SII: the influence
843 of vibrotactile amplitude during passive and task-relevant stimulation. Brain Res Cogn
844 Brain Res. 2004;19: 174–184. doi:10.1016/j.cogbrainres.2003.11.013

845 45. Staines WR, Graham SJ, Black SE, McIlroy WE. Task-relevant modulation of
846 contralateral and ipsilateral primary somatosensory cortex and the role of a prefrontal-
847 cortical sensory gating system. NeuroImage. 2002;15: 190–199.
848 doi:10.1006/nimg.2001.0953

849 46. Gomez-Ramirez M, Hysaj K, Niebur E. Neural mechanisms of selective attention in the
850 somatosensory system. J Neurophysiol. 2016;116: 1218–1231. doi:10.1152/jn.00637.2015

851 47. Scaglione A, Foffani G, Moxon KA. Spike count, spike timing and temporal information
852 in the cortex of awake, freely moving rats. J Neural Eng. 2014;11: 046022.
853 doi:10.1088/1741-2560/11/4/046022

854 48. Yu J, Gutnisky DA, Hires SA, Svoboda K. Layer 4 fast-spiking interneurons filter
855 thalamocortical signals during active somatosensation. Nat Neurosci. 2016;19: 1647–
856 1657. doi:10.1038/nn.4412

857 49. London BM, Miller LE. Responses of somatosensory area 2 neurons to actively and
858 passively generated limb movements. J Neurophysiol. 2013;109: 1505–1513.
859 doi:10.1152/jn.00372.2012

860 50. Nelson RJ. Activity of monkey primary somatosensory cortical neurons changes prior to
861 active movement. Brain Res. 1987;406: 402–407. doi:10.1016/0006-8993(87)90815-8

862 51. Bensmaia S, Helms Tillery SI. Tactile Feedback from the Hand. In: Balasubramanian R,
863 Santos VJ, editors. The Human Hand as an Inspiration for Robot Hand Development.
864 Cham: Springer International Publishing; 2014. pp. 143–157. doi:10.1007/978-3-319-
865 03017-3_7

866 52. Winship IR, Murphy TH. Remapping the somatosensory cortex after stroke: insight from
867 imaging the synapse to network. Neurosci Rev J Bringing Neurobiol Neurol Psychiatry.
868 2009;15: 507–524. doi:10.1177/1073858409333076

869 53. Ardesch DJ, Balbi M, Murphy TH. Automated touch sensing in the mouse tapered beam
870 test using Raspberry Pi. J Neurosci Methods. 2017;291: 221–226.
871 doi:10.1016/j.jneumeth.2017.08.030

872 54. Zhao C, Puurunen K, Schallert T, Sivenius J, Jolkkonen J. Effect of cholinergic
873 medication, before and after focal photothrombotic ischemic cortical injury, on
874 histological and functional outcome in aged and young adult rats. Behav Brain Res.

875 2005;156: 85–94. doi:10.1016/j.bbr.2004.05.011

876 55. Lipsanen A, Hiltunen M, Jolkkonen J. Chronic ibuprofen treatment does not affect the
877 secondary pathology in the thalamus or improve behavioral outcome in middle cerebral
878 artery occlusion rats. Pharmacol Biochem Behav. 2011;99: 468–474.
879 doi:10.1016/j.pbb.2011.04.019

880 56. Schallert T, Woodlee MT, Fleming SM. Disentangling multiple types of recovery from
881 brain injury. Pharmacol Cereb Ischemia. 2002; 201–216.

882 57. Blackwell AA, Widick WL, Cheatwood JL, Whishaw IQ, Wallace DG. Unilateral
883 forelimb sensorimotor cortex devascularization disrupts the topographic and kinematic
884 characteristics of hand movements while string-pulling for food in the rat. Behav Brain
885 Res. 2018;338: 88–100. doi:10.1016/j.bbr.2017.10.014

886 58. Romano SA, Pietri T, Pérez-Schuster V, Jouary A, Haudrechy M, Sumbre G. Spontaneous
887 Neuronal Network Dynamics Reveal Circuit's Functional Adaptations for Behavior.
888 Neuron. 2015;85: 1070–1085. doi:10.1016/j.neuron.2015.01.027

889 59. Romano SA, Pérez-Schuster V, Jouary A, Boulanger-Weill J, Candeo A, Pietri T, et al. An
890 integrated calcium imaging processing toolbox for the analysis of neuronal population
891 dynamics. PLoS Comput Biol. 2017;13: e1005526. doi:10.1371/journal.pcbi.1005526

892 60. Bauer AQ, Kraft AW, Wright PW, Snyder AZ, Lee J-M, Culver JP. Optical imaging of
893 disrupted functional connectivity following ischemic stroke in mice. NeuroImage.
894 2014;99: 388–401. doi:10.1016/j.neuroimage.2014.05.051

895 61. Blaschke SJ, Hensel L, Minassian A, Vlachakis S, Tscherpel C, Vay SU, et al. Translating
896 Functional Connectivity After Stroke: Functional Magnetic Resonance Imaging Detects
897 Comparable Network Changes in Mice and Humans. Stroke. 2021;52: 2948–2960.
898 doi:10.1161/STROKEAHA.120.032511

899 62. Carter AR, Astafiev SV, Lang CE, Connor LT, Rengachary J, Strube MJ, et al. Resting
900 interhemispheric functional magnetic resonance imaging connectivity predicts
901 performance after stroke. Ann Neurol. 2010;67: 365–375. doi:10.1002/ana.21905

902 63. Carter AR, Shulman GL, Corbetta M. Why use a connectivity-based approach to study
903 stroke and recovery of function? NeuroImage. 2012;62: 2271–2280.
904 doi:10.1016/j.neuroimage.2012.02.070

905 64. Hakon J, Quattromani MJ, Sjölund C, Tomasevic G, Carey L, Lee J-M, et al. Multisensory
906 stimulation improves functional recovery and resting-state functional connectivity in the
907 mouse brain after stroke. NeuroImage Clin. 2017;17: 717–730.
908 doi:10.1016/j.nicl.2017.11.022

909 65. Longo V, Barbati SA, Re A, Paciello F, Bolla M, Rinaudo M, et al. Transcranial Direct
910 Current Stimulation Enhances Neuroplasticity and Accelerates Motor Recovery in a

Stroke Mouse Model. Stroke. 2022; STROKEAHA121034200. doi:10.1161/STROKEAHA.121.034200

66. Olafson ER, Jamison KW, Sweeney EM, Liu H, Wang D, Bruss JE, et al. Functional connectome reorganization relates to post-stroke motor recovery and structural and functional disconnection. NeuroImage. 2021;245: 118642. doi:10.1016/j.neuroimage.2021.118642

67. Rehme AK, Grefkes C. Cerebral network disorders after stroke: evidence from imaging-based connectivity analyses of active and resting brain states in humans. J Physiol. 2013;591: 17–31. doi:10.1113/jphysiol.2012.243469

68. Siegel JS, Ramsey LE, Snyder AZ, Metcalf NV, Chacko RV, Weinberger K, et al. Disruptions of network connectivity predict impairment in multiple behavioral domains after stroke. Proc Natl Acad Sci U S A. 2016;113: E4367–E4376. doi:10.1073/pnas.1521083113

69. Silasi G, Murphy TH. Stroke and the Connectome: How Connectivity Guides Therapeutic Intervention. Neuron. 2014;83: 1354–1368. doi:10.1016/j.neuron.2014.08.052

70. Urbin MA, Hong X, Lang CE, Carter AR. Resting-state functional connectivity and its association with multiple domains of upper-extremity function in chronic stroke. Neurorehabil Neural Repair. 2014;28: 761–769. doi:10.1177/1545968314522349

71. Latifi S, Mitchell S, Habibey R, Hosseini F, Donzis E, Estrada-Sánchez AM, et al. Neuronal Network Topology Indicates Distinct Recovery Processes after Stroke. Cereb Cortex N Y NY. 2020;30: 6363–6375. doi:10.1093/cercor/bhaa191

72. Bechay KR, Abduljawad N, Latifi S, Suzuki K, Iwashita H, Carmichael ST. PDE2A Inhibition Enhances Axonal Sprouting, Functional Connectivity, and Recovery after Stroke. J Neurosci. 2022;42: 8225–8236. doi:10.1523/JNEUROSCI.0730-22.2022

73. Buzsáki G. Neural syntax: cell assemblies, synapsembles, and readers. Neuron. 2010;68: 362–385. doi:10.1016/j.neuron.2010.09.023

74. Buzsáki G, Watson BO. Brain rhythms and neural syntax: implications for efficient coding of cognitive content and neuropsychiatric disease. Dialogues Clin Neurosci. 2012;14: 345–367. doi:10.31887/DCNS.2012.14.4/gbuzsaki

75. Palm G, Knoblauch A, Hauser F, Schüz A. Cell assemblies in the cerebral cortex. Biol Cybern. 2014;108: 559–572. doi:10.1007/s00422-014-0596-4

76. Mölter J, Avitan L, Goodhill GJ. Detecting neural assemblies in calcium imaging data. BMC Biol. 2018;16: 143. doi:10.1186/s12915-018-0606-4

77. Deolindo CS, Kunicki ACB, da Silva MI, Lima Brasil F, Moioli RC. Neuronal Assemblies Evidence Distributed Interactions within a Tactile Discrimination Task in Rats. Front

946 Neural Circuits. 2017;11: 114. doi:10.3389/fncir.2017.00114

947 78. Murphy TH, Corbett D. Plasticity during stroke recovery: from synapse to behaviour. Nat
948 Rev Neurosci. 2009;10: 861–872. doi:10.1038/nrn2735

949 79. Xu X, Ye L, Ruan Q. Environmental enrichment induces synaptic structural modification
950 after transient focal cerebral ischemia in rats. Exp Biol Med Maywood NJ. 2009;234:
951 296–305. doi:10.3181/0804-RM-128

952 80. Biernaskie J, Chernenko G, Corbett D. Efficacy of rehabilitative experience declines with
953 time after focal ischemic brain injury. J Neurosci Off J Soc Neurosci. 2004;24: 1245–
954 1254. doi:10.1523/JNEUROSCI.3834-03.2004

955 81. Brown CE, Li P, Boyd JD, Delaney KR, Murphy TH. Extensive turnover of dendritic
956 spines and vascular remodeling in cortical tissues recovering from stroke. J Neurosci Off J
957 Soc Neurosci. 2007;27: 4101–4109. doi:10.1523/JNEUROSCI.4295-06.2007

958 82. Carmichael ST, Archibeque I, Luke L, Nolan T, Momiy J, Li S. Growth-associated gene
959 expression after stroke: evidence for a growth-promoting region in peri-infarct cortex. Exp
960 Neurol. 2005;193: 291–311. doi:10.1016/j.expneurol.2005.01.004

961 83. Cheatwood JL, Emerick AJ, Kartje GL. Neuronal plasticity and functional recovery after
962 ischemic stroke. Top Stroke Rehabil. 2008;15: 42–50. doi:10.1310/tsr1501-42

963 84. Ploughman M, Windle V, MacLellan CL, White N, Doré JJ, Corbett D. Brain-derived
964 neurotrophic factor contributes to recovery of skilled reaching after focal ischemia in rats.
965 Stroke. 2009;40: 1490–1495. doi:10.1161/STROKEAHA.108.531806

966 85. Carmichael ST. Plasticity of Cortical Projections after Stroke. The Neuroscientist. 2003;9:
967 64–75. doi:10.1177/1073858402239592

968 86. Carmichael ST. Cellular and molecular mechanisms of neural repair after stroke: Making
969 waves. Ann Neurol. 2006;59: 735–742. doi:10.1002/ana.20845

970 87. Dancause N. Extensive Cortical Rewiring after Brain Injury. J Neurosci. 2005;25: 10167–
971 10179. doi:10.1523/JNEUROSCI.3256-05.2005

972 88. Carmichael ST. Gene expression changes after focal stroke, traumatic brain and spinal
973 cord injuries. Curr Opin Neurol. 2003;16: 699–704.
974 doi:10.1097/01.wco.0000102621.38669.77

975 89. Li S, Carmichael ST. Growth-associated gene and protein expression in the region of
976 axonal sprouting in the aged brain after stroke. Neurobiol Dis. 2006;23: 362–373.
977 doi:10.1016/j.nbd.2006.03.011

978 90. Li S, Overman JJ, Katsman D, Kozlov SV, Donnelly CJ, Twiss JL, et al. An age-related
979 sprouting transcriptome provides molecular control of axonal sprouting after stroke. Nat

980 Neurosci. 2010;13: 1496–1504. doi:10.1038/nn.2674

981 91. Paz JT, Christian CA, Parada I, Prince DA, Huguenard JR. Focal cortical infarcts alter
982 intrinsic excitability and synaptic excitation in the reticular thalamic nucleus. J Neurosci
983 Off J Soc Neurosci. 2010;30: 5465–5479. doi:10.1523/JNEUROSCI.5083-09.2010

984 92. Staines WR, Black SE, Graham SJ, McIlroy WE. Somatosensory gating and recovery
985 from stroke involving the thalamus. Stroke. 2002;33: 2642–2651.
986 doi:10.1161/01.str.0000032552.40405.40

987 93. Carmichael ST, Wei L, Rovainen CM, Woolsey TA. New patterns of intracortical
988 projections after focal cortical stroke. Neurobiol Dis. 2001;8: 910–922.
989 doi:10.1006/nbdi.2001.0425

990 94. Tennant KA, Taylor SL, White ER, Brown CE. Optogenetic rewiring of thalamocortical
991 circuits to restore function in the stroke injured brain. Nat Commun. 2017;8: 15879.
992 doi:10.1038/ncomms15879

993 95. Brown CE, Murphy TH. Livin' on the Edge: Imaging Dendritic Spine Turnover in the
994 Peri-Infarct Zone during Ischemic Stroke and Recovery. The Neuroscientist. 2008;14:
995 139–146. doi:10.1177/1073858407309854

996 96. Ergul A, Alhusban A, Fagan SC. Angiogenesis: a harmonized target for recovery after
997 stroke. Stroke. 2012;43: 2270–2274. doi:10.1161/STROKEAHA.111.642710

998 97. Greenberg DA. Cerebral angiogenesis: a realistic therapy for ischemic disease? Methods
999 Mol Biol Clifton NJ. 2014;1135: 21–24. doi:10.1007/978-1-4939-0320-7_2

1000 98. Hatakeyama M, Ninomiya I, Kanazawa M. Angiogenesis and neuronal remodeling after
1001 ischemic stroke. Neural Regen Res. 2020;15: 16–19. doi:10.4103/1673-5374.264442

1002 99. Bullmore E, Sporns O. Complex brain networks: graph theoretical analysis of structural
1003 and functional systems. Nat Rev Neurosci. 2009;10: 186–198. doi:10.1038/nrn2575

1004 100. Sporns O. The non-random brain: efficiency, economy, and complex dynamics. Front
1005 Comput Neurosci. 2011;5: 5. doi:10.3389/fncom.2011.00005

1006 101. Stam CJ. Modern network science of neurological disorders. Nat Rev Neurosci. 2014;15:
1007 683–695. doi:10.1038/nrn3801

1008 102. Berkes P, Orbán G, Lengyel M, Fiser J. Spontaneous cortical activity reveals hallmarks of
1009 an optimal internal model of the environment. Science. 2011;331: 83–87.
1010 doi:10.1126/science.1195870

1011 103. Cossart R, Aronov D, Yuste R. Attractor dynamics of network UP states in the neocortex.
1012 Nature. 2003;423: 283–288. doi:10.1038/nature01614

1013 104. Harris KD, Csicsvari J, Hirase H, Dragoi G, Buzsáki G. Organization of cell assemblies in
1014 the hippocampus. Nature. 2003;424: 552–556. doi:10.1038/nature01834

1015 105. Hyman JM, Whitman J, Emberly E, Woodward TS, Seamans JK. Action and outcome
1016 activity state patterns in the anterior cingulate cortex. Cereb Cortex N Y N 1991. 2013;23:
1017 1257–1268. doi:10.1093/cercor/bhs104

1018 106. Malvache A, Reichinnek S, Villette V, Haimerl C, Cossart R. Awake hippocampal
1019 reactivations project onto orthogonal neuronal assemblies. Science. 2016;353: 1280–1283.
1020 doi:10.1126/science.aaf3319

1021 107. Miller JK, Ayzenshtat I, Carrillo-Reid L, Yuste R. Visual stimuli recruit intrinsically
1022 generated cortical ensembles. Proc Natl Acad Sci U S A. 2014;111: E4053-4061.
1023 doi:10.1073/pnas.1406077111

1024 108. Sakata S, Harris KD. Laminar structure of spontaneous and sensory-evoked population
1025 activity in auditory cortex. Neuron. 2009;64: 404–418. doi:10.1016/j.neuron.2009.09.020

1026 109. See JZ, Atencio CA, Sohal VS, Schreiner CE. Coordinated neuronal ensembles in primary
1027 auditory cortical columns. eLife. 7: e35587. doi:10.7554/eLife.35587

1028 110. Truccolo W, Hochberg LR, Donoghue JP. Collective dynamics in human and monkey
1029 sensorimotor cortex: predicting single neuron spikes. Nat Neurosci. 2010;13: 105–111.
1030 doi:10.1038/nn.2455

1031 111. Villette V, Malvache A, Tressard T, Dupuy N, Cossart R. Internally Recurring
1032 Hippocampal Sequences as a Population Template of Spatiotemporal Information.
1033 Neuron. 2015;88: 357–366. doi:10.1016/j.neuron.2015.09.052

1034 112. Avitan L, Pujic Z, Mölter J, Van De Poll M, Sun B, Teng H, et al. Spontaneous Activity in
1035 the Zebrafish Tectum Reorganizes over Development and Is Influenced by Visual
1036 Experience. Curr Biol CB. 2017;27: 2407-2419.e4. doi:10.1016/j.cub.2017.06.056

1037 113. Pietri T, Romano SA, Pérez-Schuster V, Boulanger-Weill J, Candat V, Sumbre G. The
1038 Emergence of the Spatial Structure of Tectal Spontaneous Activity Is Independent of
1039 Visual Inputs. Cell Rep. 2017;19: 939–948. doi:10.1016/j.celrep.2017.04.015

1040 114. Thompson AW, Scott EK. Characterisation of sensitivity and orientation tuning for
1041 visually responsive ensembles in the zebrafish tectum. Sci Rep. 2016;6: 34887.
1042 doi:10.1038/srep34887

1043 115. Luczak A, Barthó P, Harris KD. Spontaneous events outline the realm of possible sensory
1044 responses in neocortical populations. Neuron. 2009;62: 413–425.
1045 doi:10.1016/j.neuron.2009.03.014

1046 116. MacLean JN, Watson BO, Aaron GB, Yuste R. Internal dynamics determine the cortical
1047 response to thalamic stimulation. Neuron. 2005;48: 811–823.

doi:10.1016/j.neuron.2005.09.035

117. Carey LM, Matyas TA. Frequency of discriminative sensory loss in the hand after stroke in a rehabilitation setting. J Rehabil Med. 2011;43: 257–263. doi:10.2340/16501977-0662

118. Connell LA, Lincoln NB, Radford KA. Somatosensory impairment after stroke: frequency of different deficits and their recovery. Clin Rehabil. 2008;22: 758–767. doi:10.1177/0269215508090674

119. Kwakkel G, Kollen B, Lindeman E. Understanding the pattern of functional recovery after stroke: facts and theories. Restor Neurol Neurosci. 2004;22: 281–299.

120. Patel AT, Duncan PW, Lai SM, Studenski S. The relation between impairments and functional outcomes poststroke. Arch Phys Med Rehabil. 2000;81: 1357–1363. doi:10.1053/apmr.2000.9397

121. Tyson SF, Hanley M, Chillala J, Selley AB, Tallis RC. Sensory loss in hospital-admitted people with stroke: characteristics, associated factors, and relationship with function. Neurorehabil Neural Repair. 2008;22: 166–172. doi:10.1177/1545968307305523

122. Brecht M, Schneider M, Sakmann B, Margrie TW. Whisker movements evoked by stimulation of single pyramidal cells in rat motor cortex. Nature. 2004;427: 704–710. doi:10.1038/nature02266

123. Houweling AR, Brecht M. Behavioural report of single neuron stimulation in somatosensory cortex. Nature. 2008;451: 65–68. doi:10.1038/nature06447

124. Simoncelli EP, Olshausen BA. Natural image statistics and neural representation. Annu Rev Neurosci. 2001;24: 1193–1216. doi:10.1146/annurev.neuro.24.1.1193

125. Barlow H. Redundancy reduction revisited. Netw Bristol Engl. 2001;12: 241–253.

126. Holtmaat A, Bonhoeffer T, Chow DK, Chuckowree J, De Paola V, Hofer SB, et al. Long-term, high-resolution imaging in the mouse neocortex through a chronic cranial window. Nat Protoc. 2009;4: 1128–1144. doi:10.1038/nprot.2009.89

127. Blackwell AA, Banovetz MT, Qandeel, Whishaw IQ, Wallace DG. The structure of arm and hand movements in a spontaneous and food rewarded on-line string-pulling task by the mouse. Behav Brain Res. 2018;345: 49–58. doi:10.1016/j.bbr.2018.02.025

128. Inayat S, Singh S, Ghasroddashti A, Qandeel, Egodage P, Whishaw IQ, et al. A Matlab-based toolbox for characterizing behavior of rodents engaged in string-pulling. Kleinfeld D, Wassum KM, editors. eLife. 2020;9: e54540. doi:10.7554/eLife.54540

129. Blackwell AA, Köppen JR, Whishaw IQ, Wallace DG. String-pulling for food by the rat: Assessment of movement, topography and kinematics of a bilaterally skilled forelimb act. Learn Motiv. 2018;61: 63–73. doi:10.1016/j.lmot.2017.03.010

130. Kislin M, Mugantseva E, Molotkov D, Kulesskaya N, Khirug S, Kirilkin I, et al. Flat-floored Air-lifted Platform: A New Method for Combining Behavior with Microscopy or Electrophysiology on Awake Freely Moving Rodents. JoVE J Vis Exp. 2014; e51869. doi:10.3791/51869

131. Schindelin J, Arganda-Carreras I, Frise E, Kaynig V, Longair M, Pietzsch T, et al. Fiji: an open-source platform for biological-image analysis. Nat Methods. 2012;9: 676–682. doi:10.1038/nmeth.2019

132. Peron S, Chen T-W, Svoboda K. Comprehensive imaging of cortical networks. Curr Opin Neurobiol. 2015;32: 115–123. doi:10.1016/j.conb.2015.03.016

133. Hendrickson AE, White PO. Promax: A Quick Method for Rotation to Oblique Simple Structure. Br J Stat Psychol. 1964;17: 65–70. doi:10.1111/j.2044-8317.1964.tb00244.x

134. Hilgetag CC, Kötter R, Stephan KE, Sporns O. Computational Methods for the Analysis of Brain Connectivity. In: Ascoli GA, editor. Computational Neuroanatomy: Principles and Methods. Totowa, NJ: Humana Press; 2002. pp. 295–335. doi:10.1007/978-1-59259-275-3_14

135. Sporns O, Honey CJ, Kötter R. Identification and Classification of Hubs in Brain Networks. PLOS ONE. 2007;2: e1049. doi:10.1371/journal.pone.0001049

136. Chen T-W, Wardill TJ, Sun Y, Pulver SR, Renninger SL, Baohan A, et al. Ultra-sensitive fluorescent proteins for imaging neuronal activity. Nature. 2013;499: 295–300. doi:10.1038/nature12354

137. Dana H, Sun Y, Mohar B, Hulse BK, Kerlin AM, Hasseman JP, et al. High-performance calcium sensors for imaging activity in neuronal populations and microcompartments. Nat Methods. 2019;16: 649–657. doi:10.1038/s41592-019-0435-6

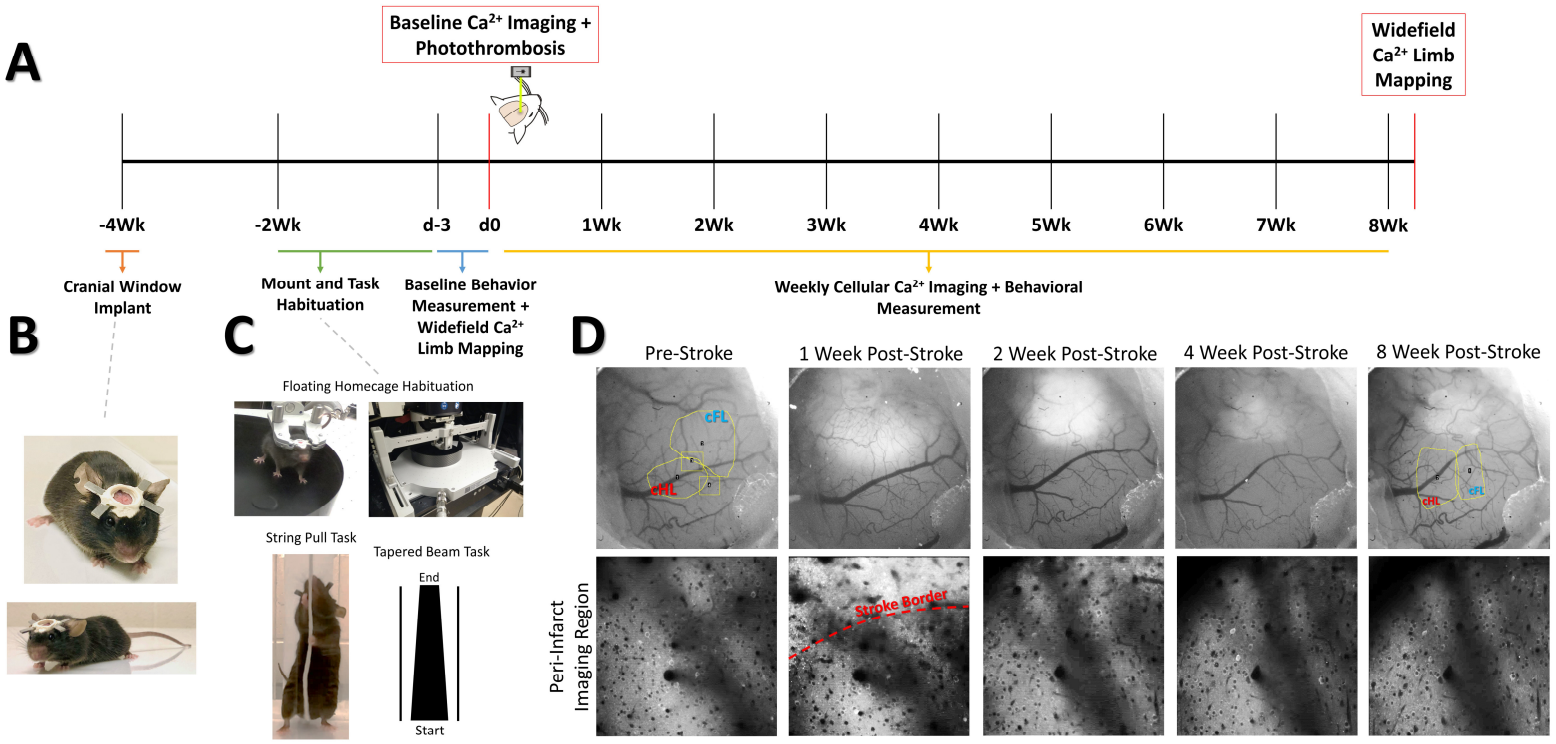
A
Baseline Ca2+ Imaging + Photothrombosis
Widefield Ca2+ Limb Mapping
-4Wk
-2Wk
d-3
d0
1Wk
2Wk
3Wk
4Wk
5Wk
6Wk
7Wk
8Wk
Cranial Window Implant
Mount and Task Habituation
Baseline Behavior Measurement + Widefield Ca2+ Limb Mapping
Weekly Cellular Ca2+ Imaging + Behavioral Measurement
B
C
Floating Homecage Habituation
String Pull Task
Tapered Beam Task
End
Start
D
Pre-Stroke
1 Week Post-Stroke
2 Week Post-Stroke
4 Week Post-Stroke
8 Week Post-Stroke
cFL
cHL
Peri-Infarct Imaging Region
Stroke Border

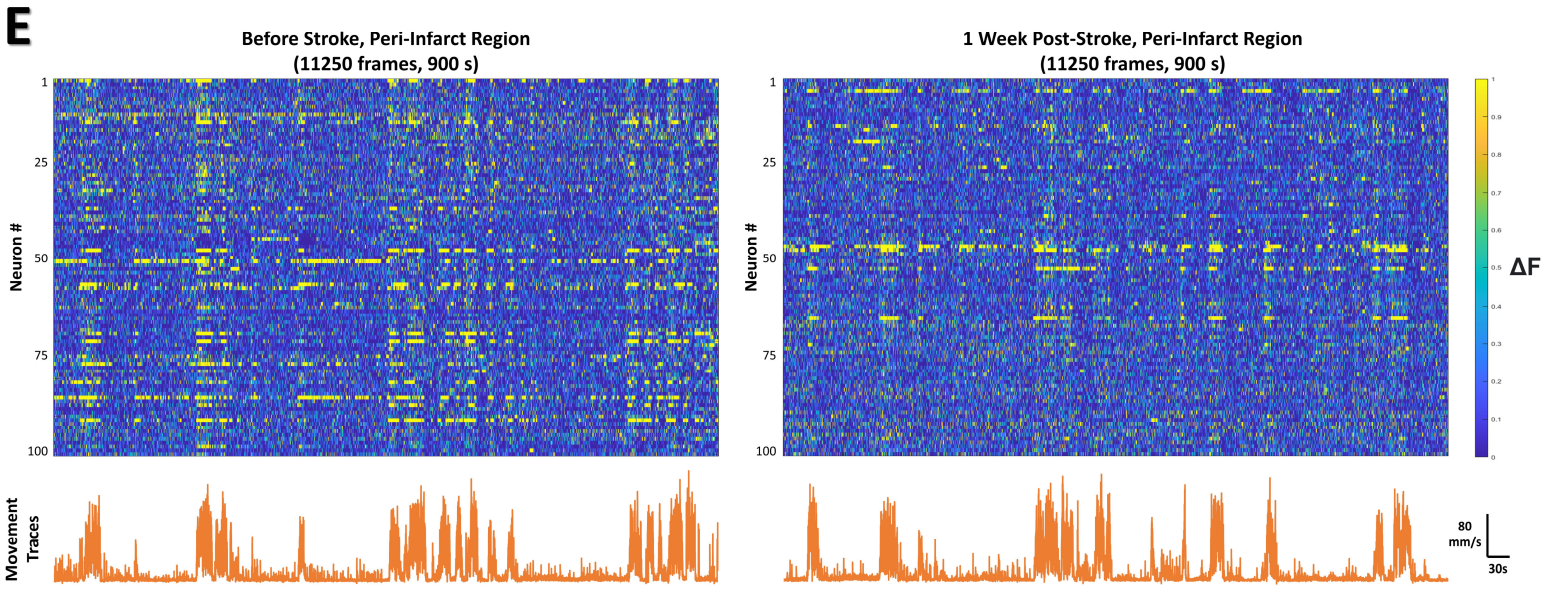
E
Before Stroke, Peri-Infarct Region
(11250 frames, 900 s)
1 Week Post-Stroke, Peri-Infarct Region
(11250 frames, 900 s)
Neuron #
1
25
50
75
100
ΔF
Movement Traces
80 mm/s
30s

1120 **Fig 1. Experimental timeline and methods.** (**A**) Timeline of experimental procedures, imaging
1121 times, and behavioral tests. (**B**) Glass cranial windows and headplates were implanted 2 weeks
1122 prior to beginning habituation protocols in Thy1-GCaMP6S mice. (**C**) Mice were habituated on
1123 the floating homecage, string pull and tapered beam for a period of 2 weeks prior to baseline
1124 measurements for behavior. Widefield Ca2+ response maps were used to determine locations for
1125 the imaging site located between the cFL and cHL sensory maps at baseline ("peri-infarct"
1126 imaging region) and imaging site lateral to the cHL at baseline ("distal" imaging region). For
1127 each Ca^{2+} imaging session, both imaging regions were imaged for a period of 15 minutes while
1128 simultaneously tracking animal movement within the mobile homecage. After baseline Ca^{2+}
1129 imaging, the somatosensory cFL map was targeted with photothrombosis. Behavioral testing on
1130 the string pull task and tapered beam task were performed weekly 1 day prior to the Ca^{2+}
1131 imaging session. After the final cellular Ca^{2+} imaging session at the 8 week time, stimulus-
1132 evoked widefield Ca^{2+} imaging was once again performed to determine the cFL and cHL
1133 somatosensory maps. (**D**) Representative widefield and two photon calcium imaging at each
1134 weekly time. The area of hyper-fluorescence due to stroke damage is apparent, with its surface
1135 area decreasing over time. (**E**) Neuron Ca^{2+} traces (ΔF) for 100 neurons from one example
1136 animal pre-stroke (left panel) and 1 week post-stroke (right panel) in the peri-infarct
1137 somatosensory imaging region. Lower line graphs demonstrate the tracked movement (mm/s)
1138 within the floating homecage corresponding to the Ca^{2+} traces above.
1139
1140
1141
1142
1143
1144
1145
1146
1147
1148
1149
1150
1151
1152
1153
1154
1155
1156
1157
1158

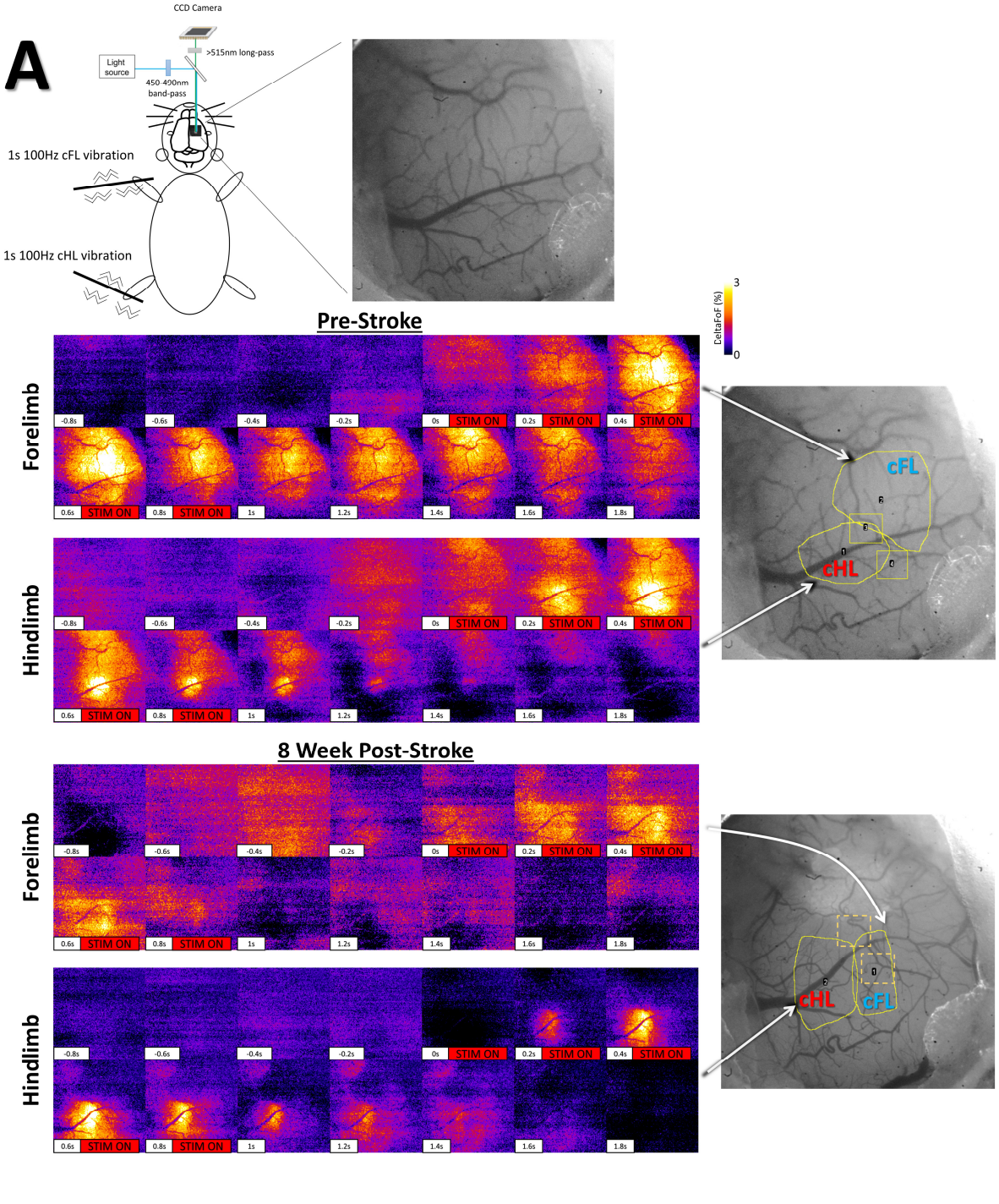
A
CCD Camera
>515nm long-pass
Light source
450-490nm band-pass
1s 100Hz cFL vibration
1s 100Hz cHL vibration
Pre-Stroke
Forelimb
Hindlimb
STIM ON
DeltaFoF (%)
3
0
cFL
cHL
8 Week Post-Stroke
Forelimb
Hindlimb
STIM ON
cHL
cFL

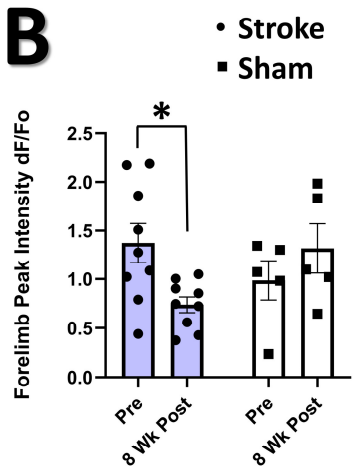
B
Stroke
Sham
Forelimb Peak Intensity dF/Fo
2.5
2.0
1.5
1.0
0.5
0.0
*
Pre
8 Wk Post
Pre
8 Wk Post

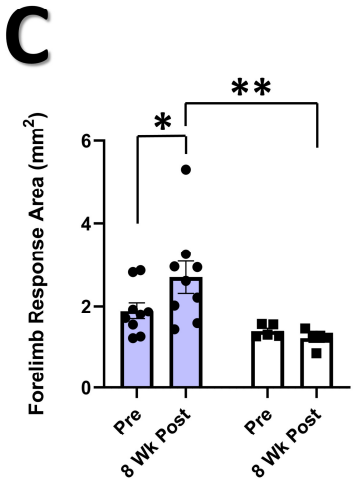
C
Forelimb Response Area (mm2)
6
4
2
0
*
**
Pre
8 Wk Post
Pre
8 Wk Post

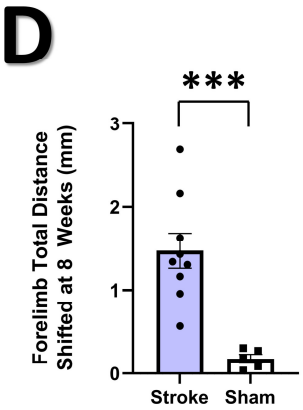
D
Forelimb Total Distance Shifted at 8 Weeks (mm)
3
2
1
0
***
Stroke
Sham

Fig 2. Photothrombotic stroke results in forelimb representation remapping onto adjacent areas of cortex and altered sensory-evoked widefield Ca^{2+} response properties at 8 weeks post-stroke. (**A**) Pseudocolored (%DeltaFoF) montages of representative cFL and cHL responses in S1 of an anesthetized animal pre-stroke and 8 week post-stroke resulting from oscillatory stimulation (1s, 100 Hz) of the cFL and cHL, respectively. At the 8 week post-stroke time, the cFL map has remapped posterior to its pre-stroke location into the area lateral to the cHL. (**B**) Mean peak forelimb Ca^{2+} transient response intensity (%DeltaFoF), measured from the thresholded cortical map area of the cFL. A significant interaction between time and stroke group was found, with *post-hoc* tests showing a significant decrease in the peak cFL response at 8-week post-stroke compared to pre-stroke ($P = 0.0143$). Mixed Effects Model, Time $F_{(1, 12)} = 0.8570$, $P = 0.3728$; Stroke Group $F_{(1, 12)} = 0.2092$, $P = 0.6556$. Interaction $F_{(1, 12)} = 8.632$, $P = 0.0124$). (**C**) Thresholded cFL response area (mm^2). A significant main effect of group and significant interaction was found, with the stroke group showing a significant enlargement in the cFL response area at 8 weeks post-stroke compared to pre-stroke ($P = 0.0152$), and a greater response area at 8 weeks in the stroke group compared to sham ($P = 0.0036$). Mixed Effects Model, Time $F_{(1, 12)} = 2.273$, $P = 0.1575$. Group $F_{(1, 12)} = 7.328$, $P = 0.0191$. Interaction $F_{(1, 12)} = 5.372$, $P = 0.0389$). (**D**) The stroke group was found to have significantly greater total distance shifted for the forelimb map at the 8 week time compared to sham ($P = 0.0002$). Stroke N = 9, Sham N = 5. *$p < 0.05$; **$p < 0.01$; ***$p < 0.001$

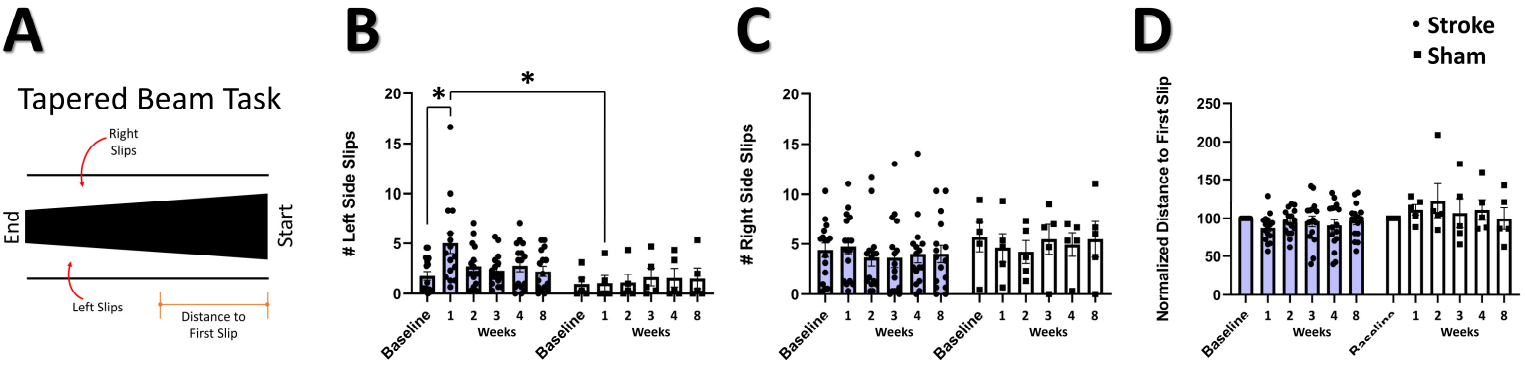
A
Tapered Beam Task
Right Slips
End
Start
Left Slips
Distance to First Slip
B
Left Side Slips
Baseline
Weeks
C
Right Side Slips
D
Stroke
Sham
Normalized Distance to First Slip

Fig 3. Impaired performance on tapered beam task after stroke. (**A**) Illustration of the tapered beam test with the three elements measured; left (contralesional) side slips, right side slips, and distance to first slip. (**B**) Mean number of left side slips. A significant interaction between time and stroke group was observed, with *post-hoc* tests showing a greater number of left side slips at 1 week in the stroke group relative to the sham group ($P = 0.0435$), and in the stroke group at 1 week relative to baseline ($P = 0.0125$). Mixed Effects Model, Time $F_{(2.007, 38.13)} = 2.178$, $P = 0.1270$; Stroke Group $F_{(1, 19)} = 2.260$; $P = 0.1492$. Interaction $F_{(5, 95)} = 2.914$, $P = 0.0172$. (**C**) Mean number of right-side slips. No main effects or interactions were observed. (**D**) Normalized distance to first slip (as % of baseline). A trend towards a main effect of group was observed, with no trends found in *post-hoc* tests. Mixed Effects Model, Time $F_{(3.135, 59.56)} = 0.6447$, $P = 0.5960$.; Stroke Group $F_{(1, 19)} = 3.030$, $P = 0.0979$; Interaction $F_{(4, 76)} = 1.242$, $P = 0.4596$). Stroke N = 16, Sham N = 5. *$p < 0.05$; **$p < 0.01$; ***$p < 0.001$

1261

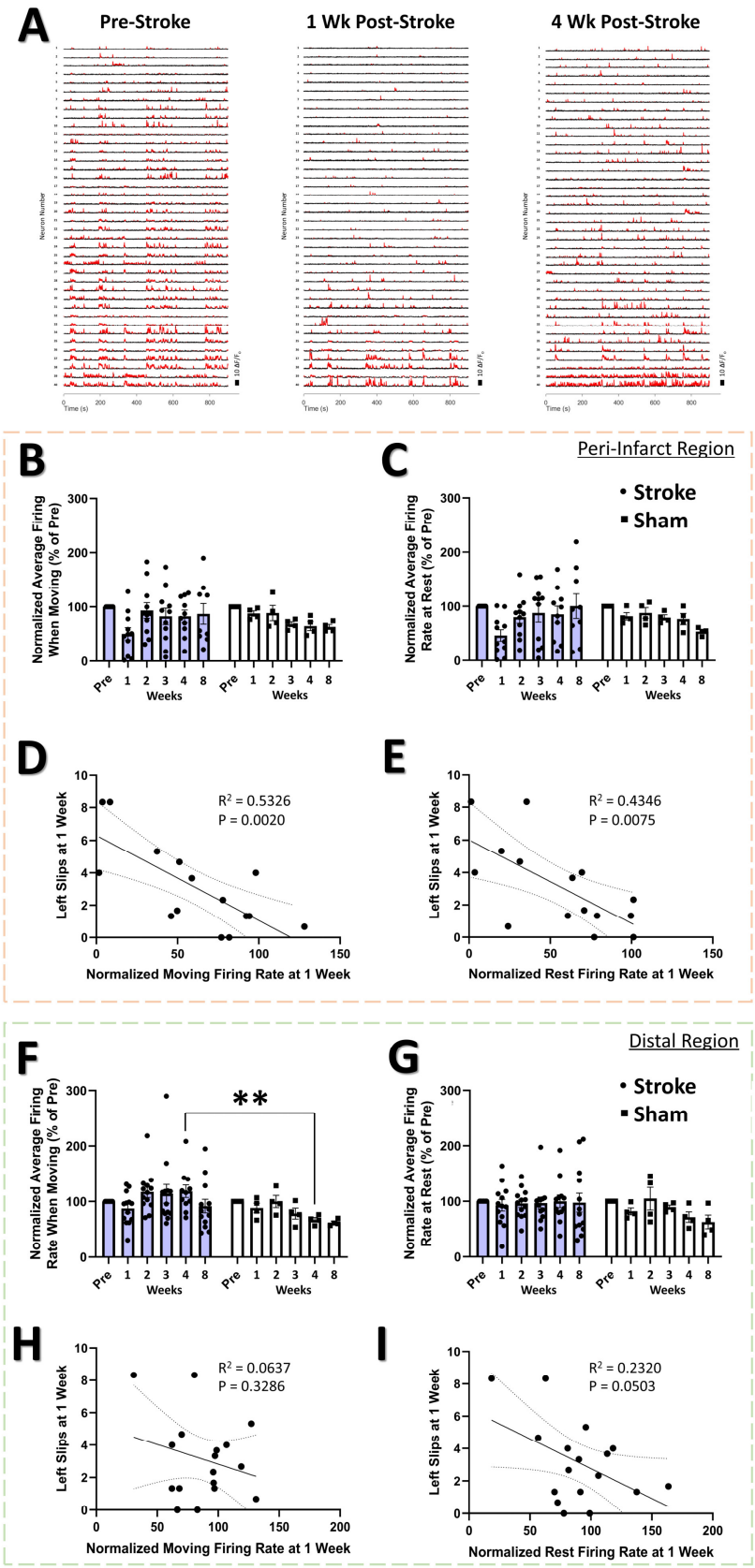
A
Pre-Stroke
1 Wk Post-Stroke
4 Wk Post-Stroke
B
Normalized Average Firing When Moving (% of Pre)
Weeks
C
Peri-Infarct Region
• Stroke
▪ Sham
Normalized Average Firing Rate at Rest (% of Pre)
D
Left Slips at 1 Week
R² = 0.5326
P = 0.0020
Normalized Moving Firing Rate at 1 Week
E
R² = 0.4346
P = 0.0075
Normalized Rest Firing Rate at 1 Week
F
Distal Region
**
Normalized Average Firing Rate When Moving (% of Pre)
G
H
R² = 0.0637
P = 0.3286
I
R² = 0.2320
P = 0.0503

Fig 4. Firing rate of neurons in the peri-infarct cortex correlates with performance on the tapered beam task. (**A**) Example Ca^{2+} traces for 40 example neurons at each time point from the peri-infarct imaging region for one example animal in the stroke group. Significant Ca^{2+} transients are highlighted by red segments. A decrease in the number of Ca^{2+} transients is visually apparent at 1 week post-stroke. (**B**) In the peri-infarct imaging region, no main effects or interaction was seen in the normalized average firing rate during animal movement, however *post-hoc* analysis indicates a trend towards decreased normalized average firing rate at 1 week in the stroke group relative to sham (P = 0.0593). Mixed Effects Model, Time $F_{(2.448, 29.99)} = 0.9487$, P = 0.4144; Stroke Group $F_{(1, 13)} = 0.04256$, P = 0.8397; Interaction $F_{(4, 49)} = 1.852$, P = 0.1339. A significant interaction was seen in the normalized average firing rate at rest (**C**), with *post-hoc* tests showing a trend towards a decrease in firing rate at rest between the stroke and sham groups at the 1 week post time (P = 0.0793, Mixed Effects Model, Time $F_{(2.240, 27.44)} = 1.048$, P = 0.3712; Stroke Group $F_{(1, 13)} = 0.006936$, P = 0.9349; Interaction $F_{(4, 49)} = 2.604$, P = 0.0471). Normalized firing rate 1 week post-stroke was negatively correlated with the number of left slips in the tapered beam at the same 1 week time during both movement ($R^2 = 0.5326$, P = 0.002) (**D**) and rest ($R^2 = 0.4346$, P = 0.0075) (**E**). In the distal imaging region, no main effects or interaction were found in the normalized average firing rate for movement (**F)** or at rest (**G**). No correlation was observed between the normalized moving firing rate at 1 week in the distal region and the number of left slips on the tapered beam ($R^2 = 0.0637$, P = 0.3286) (**H**). A statistical trend was observed towards a negative correlation between normalized firing rate at rest at 1 week with left slips on the tapered beam at the same 1 week time ($R^2 = 0.2320$, P = 0.0503) (**I**). Peri-infarct region Stroke N = 11, Sham N = 4. Distal region Stroke N = 13, Sham N = 4. *p < 0.05; **p < 0.01; ***p < 0.001

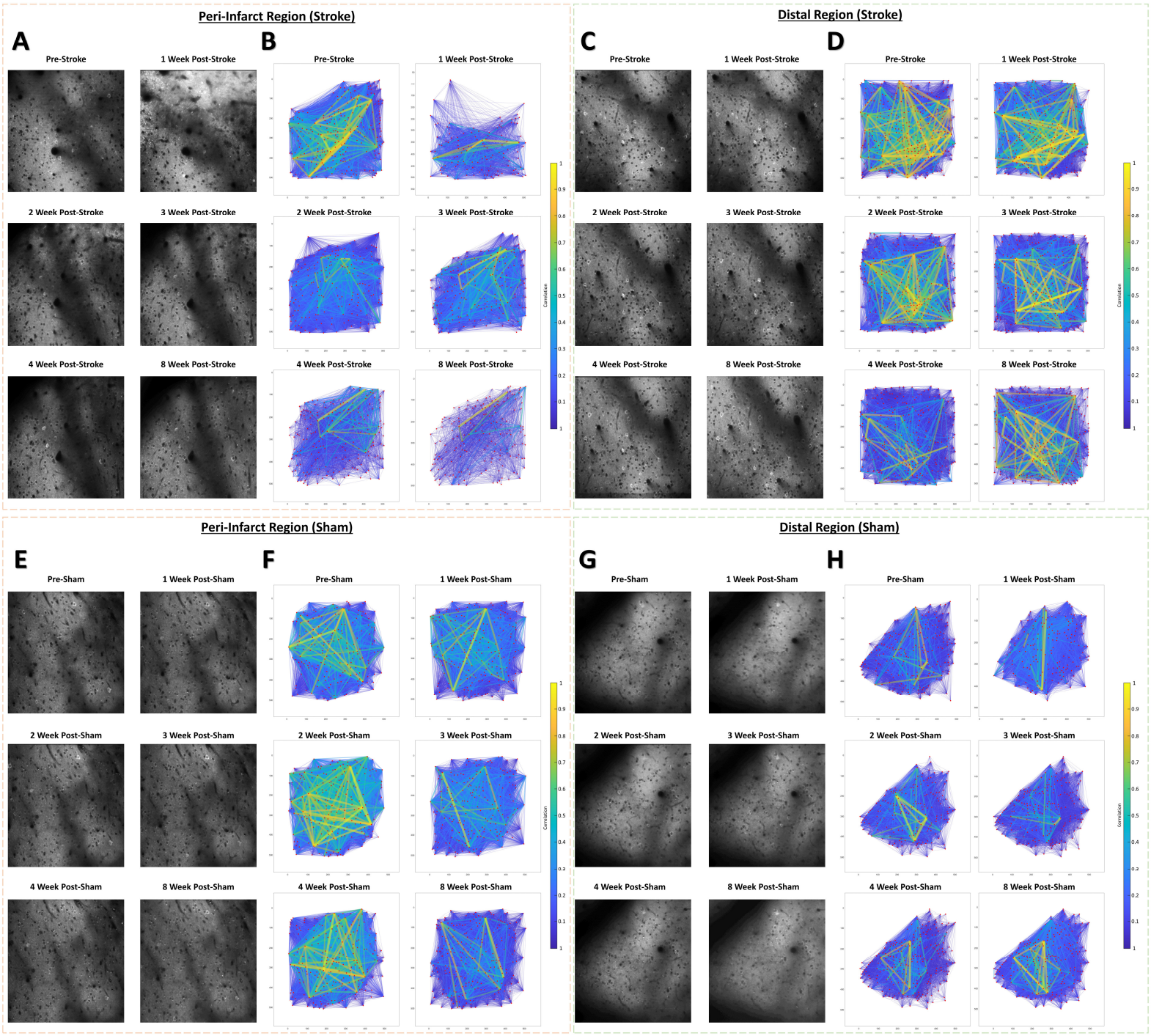
Peri-Infarct Region (Stroke)
Distal Region (Stroke)
Peri-Infarct Region (Sham)
Distal Region (Sham)
A
B
C
D
E
F
G
H
Pre-Stroke
1 Week Post-Stroke
2 Week Post-Stroke
3 Week Post-Stroke
4 Week Post-Stroke
8 Week Post-Stroke
Pre-Sham
1 Week Post-Sham
2 Week Post-Sham
3 Week Post-Sham
4 Week Post-Sham
8 Week Post-Sham
Correlation

Fig 5. Example cellular GCaMP6S Ca^{2+} fluorescence images and population functional connectivity plots. (**A-D**) Ca^{2+} fluorescence images and functional connectivity plots from the peri-infarct imaging region and the distal imaging region for one example stroke group animal. Population functional connectivity plots demonstrate neurons as red dots, and the functional connection strength as lines with color and line width determined by the strength of the correlation between neurons. Notable cortical damage is visible in the upper portion of the 1 week post-stroke Ca^{2+} fluorescence image in the peri-infarct imaging region (**A**), which notably improves over the 2-4 week times. A notable loss of functional connections and loss in the number of connections with strong correlation (>0.3) is visible in the functional connectivity plots at 1 week post-stroke in the peri-infarct imaging region (**B**). In the distal imaging region post-stroke, less structural change is visible in the cellular Ca^{2+} fluorescence images (**C**), and less change to functional connectivity of the population over time (**D**). (**E-H**) Ca^{2+} fluorescence images and functional connectivity plots from the peri-infarct imaging region and the distal imaging region for one example sham group animal. Less structural changes within the cellular Ca^{2+} fluorescence images and in the functional connectivity plots are visually apparent relative to the example stroke animal.

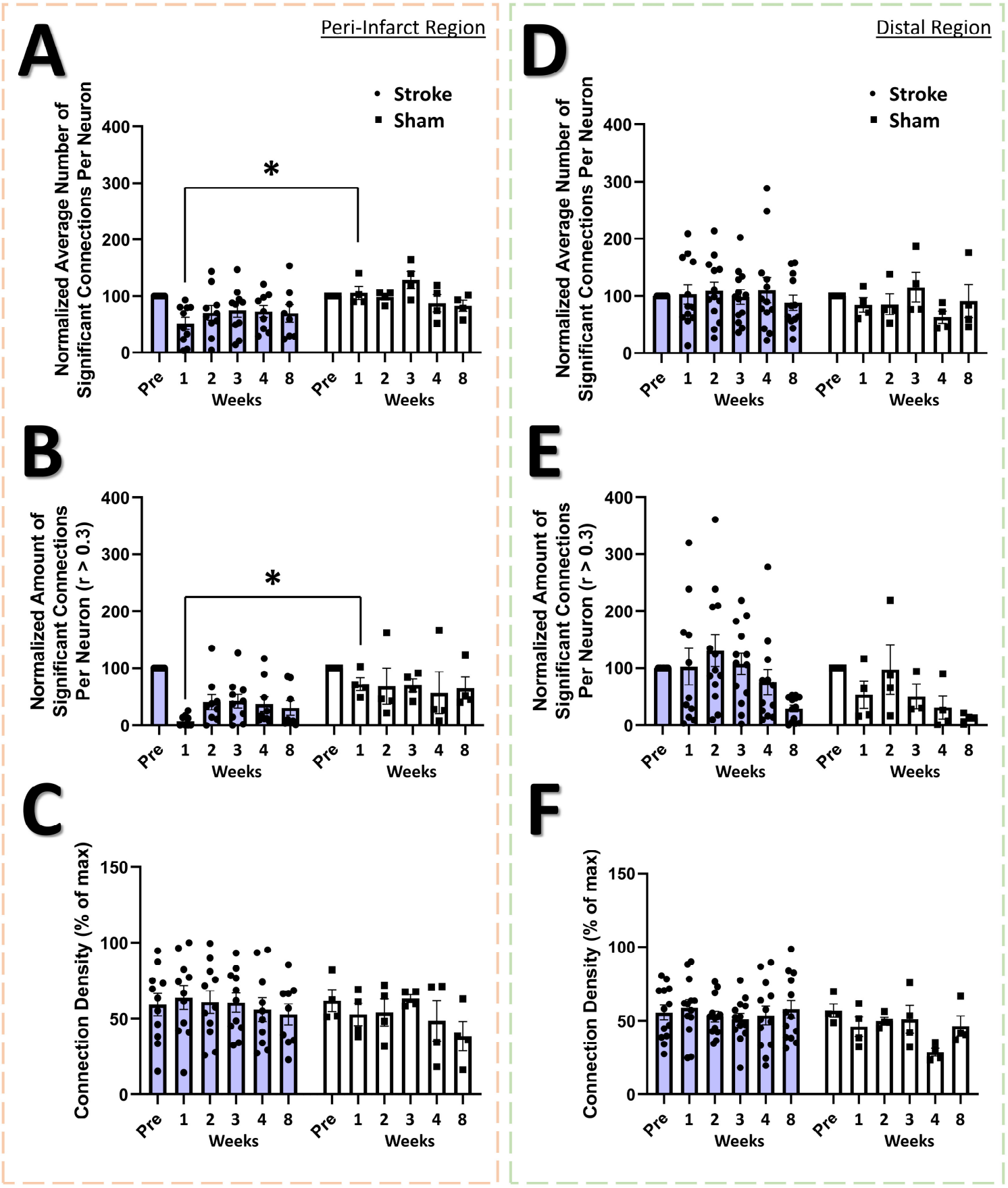
A
Peri-Infarct Region
Stroke
Sham
Normalized Average Number of Significant Connections Per Neuron
400
300
200
100
0
*
Pre 1 2 3 4 8 Pre 1 2 3 4 8
Weeks Weeks
B
Normalized Amount of Significant Connections Per Neuron (r > 0.3)
400
300
200
100
0
*
Pre 1 2 3 4 8 Pre 1 2 3 4 8
Weeks Weeks
C
Connection Density (% of max)
150
100
50
0
Pre 1 2 3 4 8 Pre 1 2 3 4 8
Weeks Weeks
D
Distal Region
Stroke
Sham
Normalized Average Number of Significant Connections Per Neuron
400
300
200
100
0
Pre 1 2 3 4 8 Pre 1 2 3 4 8
Weeks Weeks
E
Normalized Amount of Significant Connections Per Neuron (r > 0.3)
400
300
200
100
0
Pre 1 2 3 4 8 Pre 1 2 3 4 8
Weeks Weeks
F
Connection Density (% of max)
150
100
50
0
Pre 1 2 3 4 8 Pre 1 2 3 4 8
Weeks Weeks

Fig 6. Altered functional connectivity in the peri-infarct somatosensory cortex. In the peri-infarct imaging region, a trend towards a main effect of group was found in the normalized average number of significant connections per neuron (**A**), with *post-hoc* tests showing a significant decrease at the 1 week post time in the stroke group relative to sham ($P = 0.0440$, Mixed Effects Model, Time $F_{(4.132, 47.11)} = 2.217$, $P = 0.1498$; Stroke Group $F_{(1, 13)} = 4.505$, $P = 0.0551$; Interaction $F_{(4, 45)} = 1.585$, $P = 0.1947$). A significant main effect of group was found in the normalized number of significant connections per neurons with correlation greater than 0.3 (**B**), with *post-hoc* tests indicating a significant decrease at the 1 week post time in the stroke group relative to sham ($P = 0.0363$). (Time $F_{(2.102, 22.60)} = 0.3885$, $P = 0.6925$. Group $F_{(1, 13)} = 6.423$, $P = 0.0262$. Interaction $F_{(4, 43)} = 0.6512$, $P = 0.6292$). (**C**) No main effects or interactions are seen in the connection density for the peri-infarct imaging region. (Time $F_{(3.251, 40.31)} = 0.3546$, $P = 0.8015$. Group $F_{(1, 13)} = 1.257$, $P = 0.2824$. Interaction $F_{(5, 62)} = 1.146$, $P = 0.3462$). In the distal imaging region, no significant main effects or interactions are seen in the normalized number of significant connections per neuron (**D**) (Time $F_{(3.173, 46.32)} = 0.5674$, $P = 0.6487$. Group $F_{(1, 15)} = 0.3172$, $P = 0.5816$. Interaction $F_{(5, 73)} = 1.525$, $P = 0.1925$), normalized amount of significant connections with correlation greater than 0.3 (**E**) (Time $F_{(2.228, 32.86)} = 2.196$, $P = 0.1224$. Group $F_{(1, 15)} = 1.036$, $P = 0.3249$. Interaction $F_{(4, 59)} = 0.7713$, $P = 0.5482$), or in the connection density **(F)** (Time $F_{(3.467, 52.01)} = 1.299$, $P = 0.2841$. Group $F_{(1, 15)} = 2.062$, $P = 0.1715$. Interaction $F_{(5, 75)} = 1.251$, $P = 0.2942$). Peri-infarct region Stroke N = 11, Sham N = 4. Distal region Stroke N = 13, Sham N = 4. *$p < 0.05$; **$p < 0.01$; ***$p < 0.001$

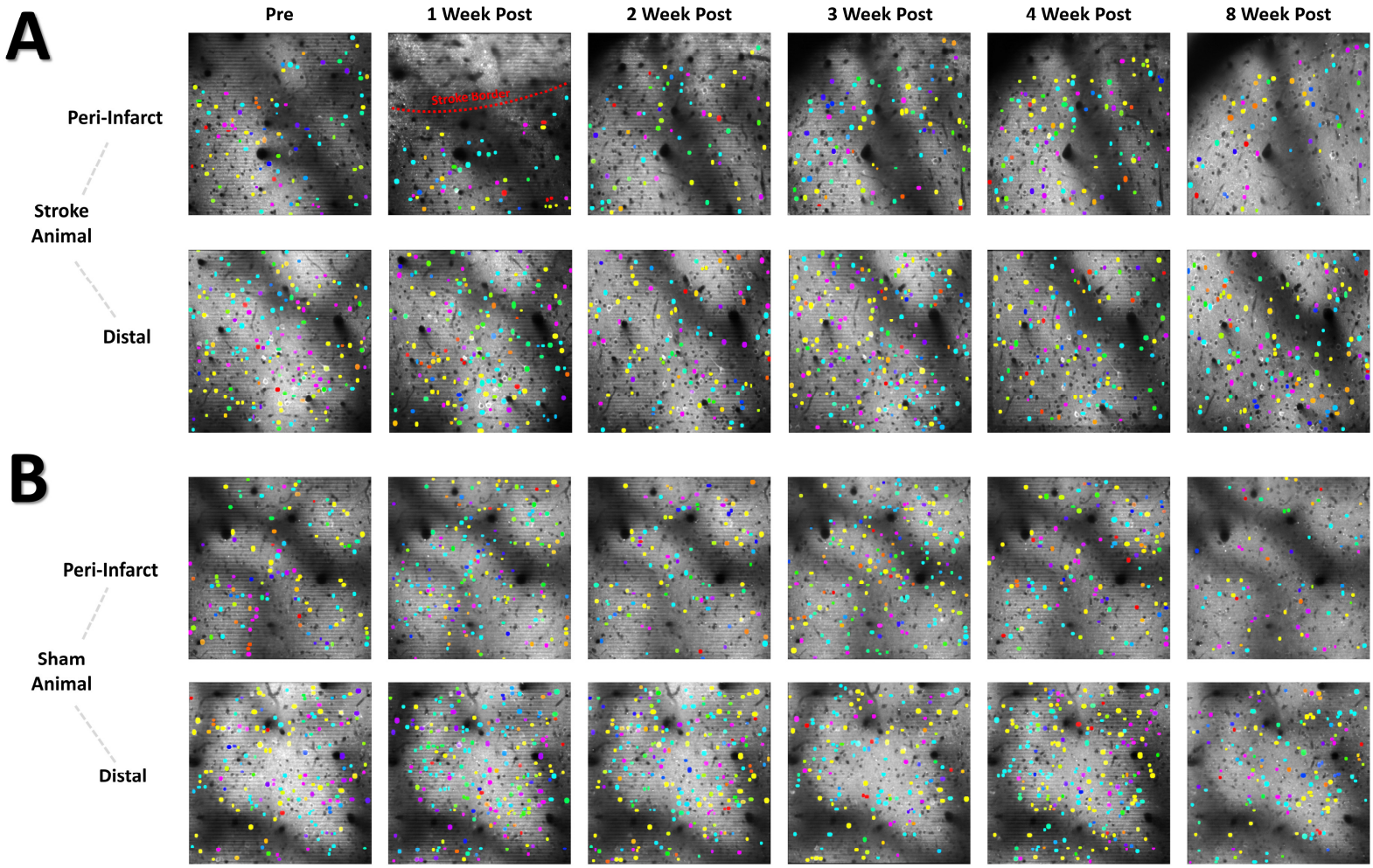
A
Pre
1 Week Post
2 Week Post
3 Week Post
4 Week Post
8 Week Post
Peri-Infarct
Stroke Animal
Distal
Stroke Border
B
Peri-Infarct
Sham Animal
Distal

Fig 7. Color coded neural assembly plots depict altered neural assembly architecture after stroke in the peri-infarct region. (**A**) Representative cellular Ca^{2+} fluorescence images with neural assemblies color coded and overlaid for each time depict a loss in the number of neural assemblies after stroke in the peri-infarct region, and a concurrent increase in the number of neurons for each remaining assembly. (**B**) Representative sham animal displays no visible change in the number of assemblies or number of neurons per assembly.

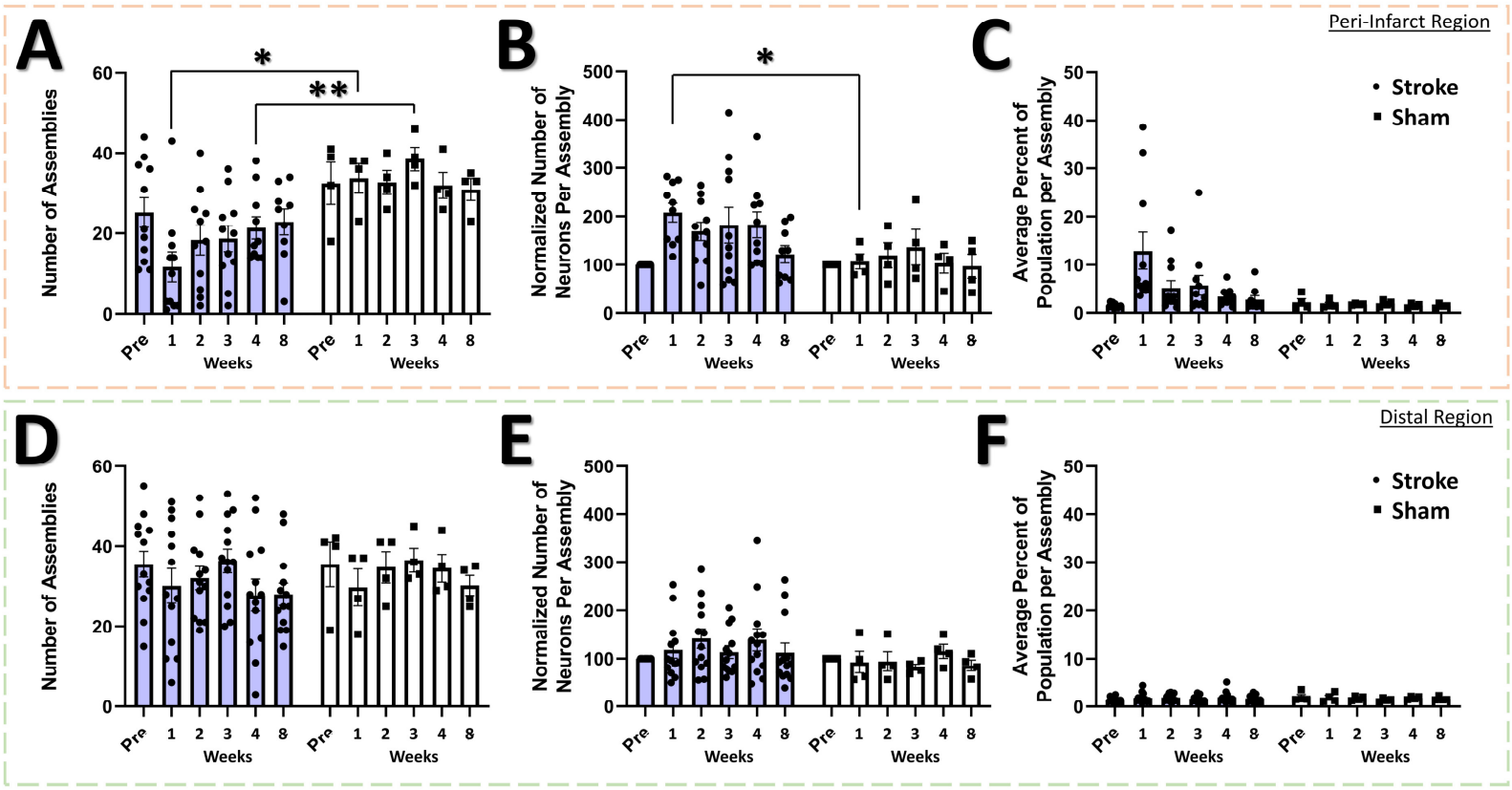
A
B
C
Peri-Infarct Region
Number of Assemblies
Normalized Number of Neurons Per Assembly
Average Percent of Population per Assembly
Stroke
Sham
Weeks
D
E
F
Distal Region

Fig 8. Neural assembly structure is disrupted in the peri-infarct region after stroke. In the peri-infarct imaging region, a significant main effect of group was found for the number of assemblies (**A**) (Time $F_{(2.883, 35.75)} = 0.8231$, $P = 0.4857$. Group $F_{(1, 13)} = 11.90$, $P = 0.0043$. Interaction $F_{(5, 62)} = 1.496$, $P = 0.2040$), with *post-hoc* tests showing a significant decrease in the number of assemblies at the 1 week and 3 week times for the stroke group compared to sham ($P = 0.0114$ & 0.0058, respectively). A statistical trend is also observed at the 2 week time for the stroke group compared to sham ($P = 0.0589$). A trend towards a main effect of group was found in the normalized number of neurons per assembly (**B**, Mixed Effects Model, Time $F_{(2.361, 28.80)} = 2.185$, $P = 0.1234$; Stroke Group $F_{(1, 13)} = 3.694$, $P = 0.0768$; Interaction $F_{(5, 61)} = 1.202$, $P = 0.3192$), with *post-hoc* tests showing a significant increase in the normalized number of neurons per assembly at 1 week for the stroke group compared to sham ($P = 0.0124$). A trend towards a main effect of group was found in the average percent of the population per assembly (**C**, Time $F_{(1.711, 21.22)} = 1.738$, $P = 0.2023$; Stroke Group $F_{(1, 13)} = 3.807$, $P = 0.0729$. Interaction $F_{(5, 62)} = 1.765$, $P = 0.1333$), with *post-hoc* tests showing a trend towards an increase in the stroke group relative to sham at the 1 week post time ($P = 0.0863$). No main effects or interaction was observed in the distal imaging region for number of assemblies (**D**), normalized number of neurons per assembly (**E**), or average percent of the population per assembly (**F**). Peri-infarct region Stroke N = 11, Sham N = 4. Distal region Stroke N = 13, Sham N = 4. *$p < 0.05$; **$p < 0.01$; ***$p < 0.001$

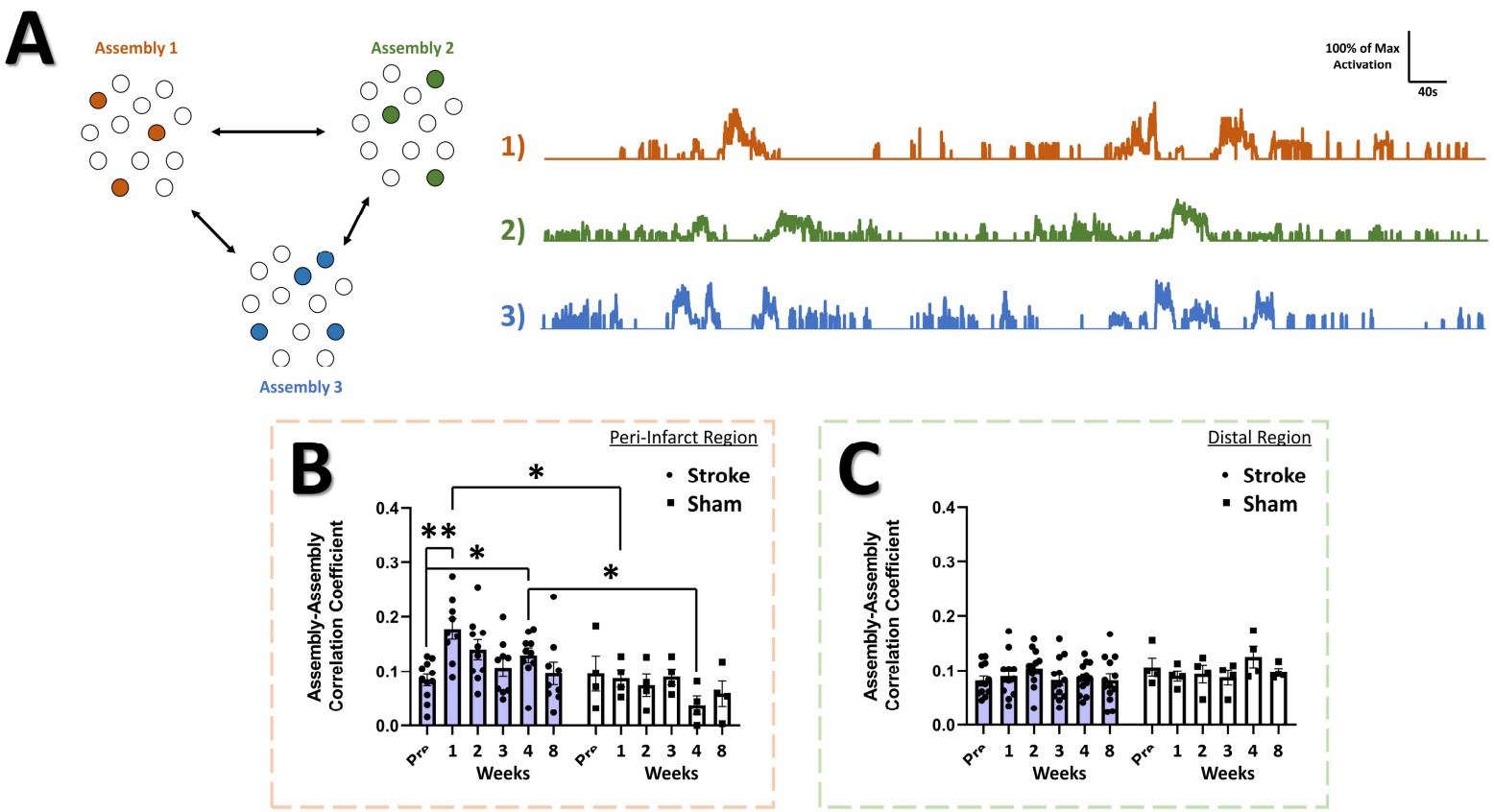
A
Assembly 1
Assembly 2
Assembly 3
100% of Max Activation
40s
1)
2)
3)
B
Peri-Infarct Region
Stroke
Sham
Assembly-Assembly Correlation Coefficient
0.4
0.3
0.2
0.1
0.0
**
*
*
*
Pre
1
2
3
4
8
Weeks
C
Distal Region
Stroke
Sham
Assembly-Assembly Correlation Coefficient
Weeks

Fig 9. Correlation among neural assemblies is increased in the peri-infarct imaging region after stroke. (**A**) Illustration of three example color coded neural assemblies from a neural population and their corresponding time series activations that were correlated. In the peri-infarct imaging region, a significant main effect of group was found in the correlation coefficient for significantly correlated assembly-assembly pairs (**B**, Mixed Effects Model, Time $F_{(3.718, 42.39)} = 2.014$, $P = 0.1141$; Stroke Group $F_{(1, 13)} = 9.155$, $P = 0.0097$. Interaction $F_{(5, 57)} = 2.348$, $P = 0.0524$), with *post-hoc* tests indicating a significantly higher correlation at 2 week ($P = 0.029$) and 4 weeks ($P = 0.0253$) in the stroke group relative to sham, and at 1 week ($P = 0.0084$) and 4 week ($P = 0.0261$) in the stroke group compared to pre-stroke. In the distal imaging region, no significant main effects or interaction was found for the correlation coefficient for significantly correlated assembly-assembly pairs (**C**). Peri-infarct region Stroke N = 11, Sham N = 4. Distal region Stroke N = 13, Sham N = 4. *$p < 0.05$; **$p < 0.01$; ***$p < 0.001$